

1 **Understanding hydrologic controls of sloping soil**
2 **response to precipitation through Machine Learning**
3 **analysis applied to synthetic data**

4 Daniel Camilo Roman Quintero¹, Pasquale Marino¹, Giovanni
5 Francesco Santonastaso¹, Roberto Greco¹

6 ¹Dipartimento di ingegneria, Università degli Studi della Campania ‘Luigi Vanvitelli’,
7 via Roma 9, 81031 Aversa (CE), Italy;

8 *Correspondence to:* Daniel Camilo Roman Quintero
9 (danielcamilo.romanquintero@unicampania.it)

10 **Abstract:**

11 Soil and underground conditions prior to the initiation of rainfall events control
12 the hydrological processes that occur in slopes, affecting the water exchange
13 through their boundaries. The present study aims at identifying suitable variables
14 to be monitored to predict the response of sloping soil to precipitation. The case
15 of a pyroclastic coarse-grained soil mantle overlaying a karstic bedrock in the
16 Southern Apennines (Italy) is described. Field monitoring of stream level
17 recordings, meteorological variables, and soil water content and suction has been
18 carried out for few years. To enrich the field dataset, a synthetic series of 1000
19 years has been generated with a physically based model coupled to a stochastic
20 rainfall model. Machine Learning techniques have been used to unwrap the non-
21 linear cause-effect relationships linking the variables. The k-means clustering
22 technique has been used for the identification of seasonally recurrent slope
23 conditions, in terms of soil moisture and groundwater level, and the Random
24 Forest technique has been used to assess how the conditions at the onset of
25 rainfall controlled the attitude of the soil mantle to retain much of the infiltrating
26 rainwater. The results show that the response in terms of the fraction of rainwater
27 remaining stored in the soil mantle at the end of rainfall events is controlled by

28 soil moisture and groundwater level prior to the rainfall initiation, giving
29 evidence of the activation of effective drainage processes.

30 **Keywords:** Water storage, slope response, underground antecedent conditions,
31 hydrological controls, Random Forest, k-means clustering

32 **1. Introduction**

33 Slope response to precipitation is highly non-linear, in terms of runoff generation,
34 rainwater infiltration and subsurface drainage processes, which are mostly
35 depending on the initial soil moisture state at the onset of each rainfall event
36 (Tromp-Van Meerveld and McDonnell, 2006b; Nieber and Sidle, 2010; Damiano
37 et al., 2017). The initial (or antecedent) conditions are related to hydrological
38 processes that occur in the slopes, which control how they exchange water with
39 the surrounding systems (i.e., atmosphere, surface water, deep groundwater).
40 These processes occur through the boundaries of the slope, and often evolve over
41 timescales of weeks or even months, much longer than the duration of rainfall
42 events, typically ranging between some hours and few days.

43 While the importance of soil moisture conditions on slope runoff and drainage
44 has been recognized long since (Ponce and Hawkins, 1996; Tromp-Van
45 Meerveld and McDonnell, 2006a, 2006b), only recently the scientific community
46 started providing new perspectives to better understand hydrologic conditions
47 predisposing slopes to landslides (Bogaard and Greco, 2018; Greco et al., 2023),
48 to explain why most of large rain events do not destabilize slopes, while only
49 some do (Bogaard and Greco, 2016), and physically based models capable of
50 integrating hydrological knowledge for predicting landslide occurrence have
51 been proposed (e.g., Bordoni et al., 2015; Greco et al., 2018; Marino et al., 2021).

52 The triggering of some rainfall-induced geohazards, such as shallow landslides
53 and debris flows, is favoured by pore pressure increase, caused by rainwater
54 infiltration and consequent soil moisture accumulation. The storage of rainwater

55 within the soil requires drainage mechanisms developing in the slopes in response
56 to precipitation to be not so effective to drain out much of the infiltrating water
57 (Greco et al., 2021; 2023). Consequently, especially for nowcasting and early
58 warning purposes, the identification of hydrological variables suitable to identify
59 slope predisposing conditions is extremely useful. Thus, to better understand how
60 hydrological predisposing conditions may control the processes involving the
61 sloping soil response in terms of water storage, field monitoring for the
62 assessment of the slope water balance is highly recommended (Bogaard and
63 Greco, 2018; Marino et al., 2020a).

64 The identification of suitable variables to be monitored in the field is indeed
65 useful to achieve an insight of the behaviour of the interconnected hydrological
66 systems (i.e., groundwater, surface water, soil water). Besides the study
67 of rainfall-induced landslides, the evaluation of the hydrological scenarios in a
68 region of interest could impact several other applications, from flood hazard
69 assessment (Reichenbach et al., 1998; Forestieri et al., 2016; Chitu et al., 2017),
70 to the prediction of possible crop water stress conditions in relation to defoliation
71 (Capretti and Battisti, 2007), pathogen expansions in chestnut grove (Gao and
72 Shain, 1995), and plant mortality in a climate change context (McDowell et al.,
73 2008).

74 This research focuses on a case study of a slope located in Campania (southern
75 Italy), in an area frequently hit by destructive rainfall-triggered shallow
76 landslides. Such geohazards are recurrent along the carbonate slopes covered
77 with unsaturated pyroclastic deposits typical of the area (Fiorillo et al., 2001;
78 Revellino et al., 2013). The underlying limestone bedrock, densely fractured, is
79 characterised by the presence of deep karst aquifers (Allocca et al., 2014). The
80 triggering mechanism of landslides in the area is the increase of water storage
81 within the soil mantle after intense and persistent precipitation, leading to pore
82 pressure build up (Bogaard and Greco 2016). Slope equilibrium is in fact

83 guaranteed by the additional shear strength promoted by soil suction (Lu and
84 Likos 2006; Greco and Gargano 2015), which reduction often leads to slope
85 failure due to shear strength loss by soil wetting during rainwater infiltration
86 (Olivares and Picarelli, 2003; Damiano and Olivares, 2010; Pagano et al., 2010;
87 Pirone et al., 2015).

88 Recent studies show that the response of the soil mantle to precipitation in the
89 study area is affected not only by rainfall characteristics and antecedent soil
90 moisture, but also by the wetness of the interface with the underlying bedrock,
91 which controls the leakage of water into the underlying fractured limestone
92 (Marino et al., 2020a; 2021). At the contact between soil and bedrock, intense
93 weathering modifies the physical properties of the soil as well as of the fractured
94 bedrock, which form a hydraulically interconnected system, the epikarst (e.g.,
95 Perrin et al., 2003; Hartmann et al., 2014; Dal Soglio et al., 2020). The changing
96 hydraulic behaviour of the soil-bedrock interface can be related to the storage of
97 water in the epikarst, where a perched aquifer forms during the rainy season
98 (Greco et al., 2014, 2018).

99 The aim of this study is to identify the major hydrological processes controlling
100 the response of the slope soil mantle to precipitation, and the seasonally recurrent
101 conditions that affect its attitude to retain much of the infiltrating rainwater,
102 through suitable measurable variables. To this aim, a rich dataset of measured
103 rainfall events and corresponding hydrological effects would be required, which
104 was not available for the case study, where monitoring activities had been carried
105 out for few years. Therefore, a synthetic 1000 years hourly dataset was generated,
106 by means of a stochastic rainfall model and a simplified physically based model
107 of the slope, coupling the unsaturated pyroclastic soil mantle and the underlying
108 perched aquifer (Greco et al., 2018). Both models had been previously calibrated
109 and validated on field experimental data (Damiano et al, 2012; Greco et al., 2013;
110 Comegna et al., 2016; Marino et al., 2021). The synthetic data of soil suction,

111 water content and aquifer water level, all measurable in the field and assumed as
112 representative of real conditions, were analysed as if they were measured data.
113 After sorting the rainfall events within the 1000 years timeseries, a dataset was
114 built with the antecedent conditions one hour before the beginning of each rainfall
115 event. It included the previously listed variables plus the total event rainfall
116 depth, and the change in the water stored in the soil mantle at the end of each
117 rainfall event. To disentangle the non-linear processes controlling the hydraulic
118 behaviour of the slope, and their role on the soil response to precipitation, the
119 dataset was analysed with Machine Learning (ML) techniques, i.e., clustering,
120 and random forest. Indeed, ML allows managing big amounts of data, such as
121 those provided by assimilation of extensive monitoring networks, remote
122 sensing, satellite products and other sources, without introducing any
123 mathematical model structure to highlight the cause-effect relationships linking
124 the variables.

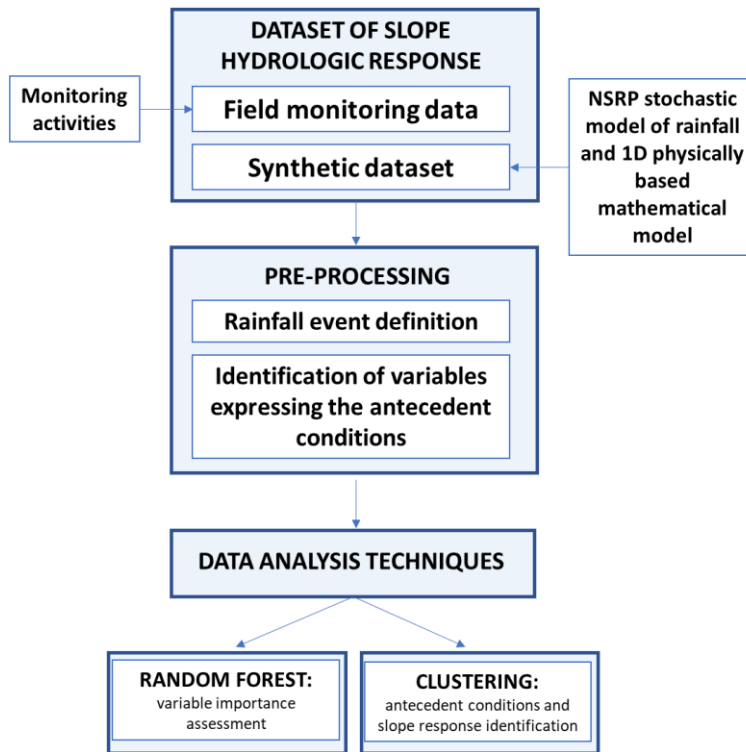
125

126 **2. Materials and methods**

127 The studied slope, described in section 2.1, belongs to the Partenio Massif, and it
128 has the typical characteristics of many pyroclastic slopes of Campania (southern
129 Italy) (Greco et al., 2018). Indeed, three major zones characterized by unsaturated
130 pyroclastic deposits can be identified in Campania (Cascini et al., 2008):
131 Campanian Apennine chain, composed by carbonate rock covered by a variable
132 layer of pyroclastic soil (from 0.1 to 5 m); Phlegraean district, formed by
133 underlying densely fractured volcanic tuff bedrock, placed under several meters
134 of pyroclastic soils; and Sarno and Picentini Mountains, where a thin layer of
135 pyroclastic material is over a terrigenous bedrock. In these three areas, the
136 thickness of the soil mantle is quite variable, according to the slope inclination
137 and to the distance from the eruptive centre (De Vita et al., 2006; Tufano et al.,
138 2021).

139 To identify the seasonally recurrent conditions that affect the attitude of the soil
140 mantle to retain much of the infiltrating water, a large set of measurements of
141 rainfall events, and their effects on the slope, would be required. Hence, to enrich
142 the data available from the monitoring activities carried out for some years at the
143 slope (Marino et al., 2020a), a synthetic dataset of the hydrologic response of the
144 slope to precipitation, has been generated with a NSRP stochastic model of
145 rainfall (Rodriguez-Iturbe et al., 1987) and a simplified 1D model of the
146 interaction of the unsaturated pyroclastic soil mantle with the underlying perched
147 aquifer forming in the epikarst. Both the models, described in the following
148 sections, had been previously developed based on experimental data (Greco et
149 al., 2013; 2018; Marino et al., 2021). The obtained synthetic dataset has been
150 compared to the limited dataset from field monitoring, showing a reasonable
151 agreement. Therefore, it has been considered suitable to reproduce slope response
152 to climate forcing, in terms of soil volumetric water content and perched aquifer
153 water level, in the studied area (see Section 2.2).

154 The synthetic dataset has been analysed with Machine Learning techniques
 155 (Section 2.3), as they result quite powerful to identify non-linear cause-effect
 156 relationships between variables, without introducing any model structure, as if
 157 the data were provided by field measurements. Figure 1 shows the flowchart of
 158 the entire methodology.

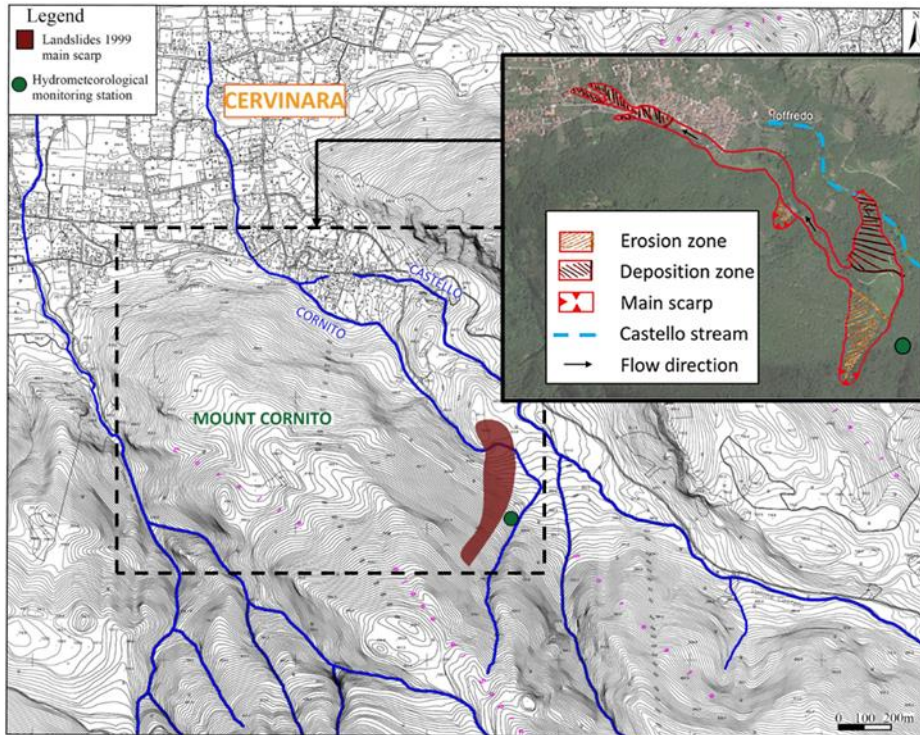


159
 160 **Figure 1. Flowchart summarizing the methodology followed in the analysis**
 161 **of sloping soil response to precipitation.**

162 **2.1. Case study**

163 The study area refers to the north-east slope of Monte Cornito, part of the Partenio
 164 Massif (Campania, southern Italy), 2 km from the town of Cervinara, about 40
 165 km northeast of the city of Naples. The slope was involved in a series of rapid
 166 shallow landslides after a rainfall event of 325 mm in 48 hours during the night
 167 between 15–16 December 1999, causing casualties and heavy damages (Fiorillo
 168 et al., 2001). A field monitoring station was installed nearby the big landslide

169 scarp since 2001. Further details of the investigated zone, with indications of the
170 area affected by the largest of the landslides triggered in 1999, are shown in
171 Figure 2.



172
173 **Figure 2. Location of the study area and indication of the zone affected by a large**
174 **landslide in 1999**

175 Partenio Massif is part of the southern Apennines area. The bedrock mainly
176 consists of Mesozoic-Cenozoic fractured limestones, mantled by loose
177 pyroclastic deposits, resulting from the explosive volcanic activity of Somma-
178 Vesuvius and Phlegrean Fields, which occurred over the last 40.000 years
179 (Rolandi et al., 2003).

180 The fractured limestone formations of the southern Apennines often host large
181 karst aquifers, through which a basal groundwater circulation occurs, for which
182 regional groundwater recharge between 100 and 500 mm/year has been
183 estimated, with 200 mm/year regarding the area of Cervinara (Allocca et al.,

184 2014). Moreover, recent studies showed that, in the upper part of the karst system,
185 denoted as epikarst (Hartmann et al., 2014), more permeable and porous than the
186 underlying rock, a perched aquifer often develops (Williams, 2008; Celico et al.,
187 2010). It temporally stores water and favors the recharge of the deep aquifer
188 through the larger fracture system. The water, which is accumulated temporally
189 in the epikarst, also reappears at the surface in small ephemeral streams.

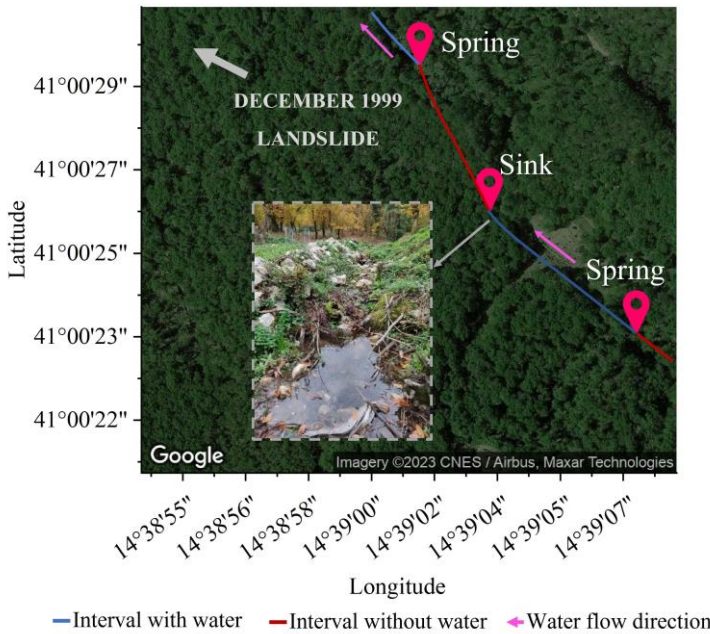
190 Specifically, the slope of Cervinara has an inclination between 35° and 50°, at an
191 elevation between 500 m and 1200 m above sea level. The soil mantle, usually
192 in unsaturated conditions, is the result of the air-fall deposition of the materials
193 from several eruptions, so it is generally layered. It mainly consists of layers of
194 volcanic ashes (with particle size in the range of sands to loamy sands) alternating
195 with pumices (sandy gravels), laying upon the densely fractured limestone
196 bedrock. Near the soil-bedrock interface, a layer of weathered ashes,
197 characterized by finer texture (silty sand), with lower hydraulic conductivity,
198 moderate plasticity and low cohesion, is often observed (Damiano et al., 2012).

199 The soil mantle thickness varies spatially from a minimum of 1.0 m, in the
200 steepest part of the slope, to larger values at its foot (up to 4-5 meters). The thin
201 soil mantle, compared to the slope width and length of hundreds of meters (Figure
202 2), makes the flow processes nearly one-dimensional, except for the close
203 proximity to geometric singularities.

204 The pyroclastic soils of the profile are characterized by high porosity (from about
205 50% for the pumices, to 75% for the ashes) and quite high values of saturated
206 hydraulic conductivity (ranging up to the order of 10^{-5} m/s). Thus, this kind of
207 soil lets rainwater infiltrate even during the most intense rainfall events, with little
208 runoff generation, and it can store a large amount of water without approaching
209 saturation. The values of soil capillary potential, measured during the rainy

210 season, rarely exceed -0.5 m, as observed also in other slopes of the area (Cascini
211 et al., 2014; Comegna et al., 2016; Napolitano et al., 2016).

212 The climate is Mediterranean, which is characterized by dry and warm summer
213 and rainy autumn and winter, with mean annual precipitation of about 1600 mm,
214 mostly occurring between October and April. The total potential
215 evapotranspiration ET_0 , estimated with the Thornthwaite formula (Shuttleworth,
216 1993), is between 700 mm and 800 mm in the altitude range between 750 m and
217 400 m (Greco et al., 2018). The vegetation mainly consists of widespread
218 deciduous chestnuts, with a dense understory of brushes and ferns, growing
219 during the flourishing period (between May and September). In fact, visual
220 inspections of the soil profile showed a large amount of organic matter and roots.
221 In most cases, roots are denser in the uppermost part of the soil mantle and
222 become sparse between the depth of 1.50 m and 2.00 m below the ground surface,
223 reaching the basal limestones and penetrating the fractures.



224
225 **Figure 3. Identification of surface water flow in the Castello stream at the beginning**
226 **of the rainy season in November 2021 by visual recognition of springs and sinks in**
227 **the watercourse**

228 Moreover, in the surrounding area, several ephemeral and perennial springs are
229 present, mostly located at the foot of the slopes, which supply a network of small
230 creeks and streams, allowing to show the activity of the aquifer discharge to the
231 surface water. An indication regarding the Castello stream (the main stream for
232 this side of the basin), with springs, is shown in Figure 3, where, during a field
233 recognition in November 11th 2021, the surface water flow appeared (springs)
234 and disappeared (sinks) in some points along the stream course. Normally the
235 stream exhibits its lowest water depth values up to the beginning of the late
236 autumn (Marino et al., 2020a, p.3.3), but it is interesting to note that the surface
237 water in the stream emerging from the epikarstic springs is an indicator of the
238 active slope drainage.

239 **2.1.1. Field monitoring data**

240 Several hydrological monitoring activities have been carried out at the slope of
241 Cervinara since 2001, initially consisting of measurements of precipitation and
242 manual readings (every two weeks) of soil suction by “Jet-fill” tensiometers,
243 equipped with a Bourdon manometer (Damiano et al., 2012). Afterwards, since
244 November 2009, an automatic monitoring station has been set at an elevation of
245 585 m a.s.l., near a narrow track close to the landslide scarp of December 1999.
246 The installed instrumentation consisted of tensiometers, time domain
247 reflectometry (TDR) probes for water content measurements, and a rain gauge
248 (Greco et al., 2013; Comegna et al., 2016).

249 Since 2017, the hydro-meteorological monitoring was enriched (Marino et al.,
250 2020a), aiming at understanding the seasonal behaviour of the slope and the
251 interactions between the hydrological systems, i.e., the unsaturated soil mantle,
252 the epikarst, and the underlying fractured bedrock.

253 Specifically, the data collected by tensiometers and TDR probes were
254 supplemented with those from a meteorological station (composed by a thermo-

255 hygrometer, a pyranometer, an anemometer, a thermocouple for soil temperature
256 measurement, and a rain gauge), and with the water level in two streams at slope
257 foot, so to gain useful information for the assessment of the water balance of the
258 studied slope.

259 The data from field monitoring , carried out between 2017 and 2020 with hourly
260 resolution, consist of rainfall, evapotranspiration, soil moisture and suction at
261 various depths, and the water depth of the Castello stream. The data have been
262 useful to highlight seasonally recurrent soil moisture distributions. More details
263 about the measured data and the observed recurrent seasonal behaviour of the
264 area of Cervinara can be found in Marino et al. (2020a).

265 **2.2. Synthetic dataset**

266 Aiming at identifying suitable variables to be monitored in the field for the
267 identification of the conditions controlling different slope responses to the
268 precipitation, a rich dataset of rainfall and underground monitored variables, such
269 as soil moisture and groundwater level, is needed. However, a complete field
270 monitored dataset is not always possible to be analyzed and, when it exists, it is
271 commonly available for short periods, granting a relatively low measurement
272 density. Hence, a synthetic dataset, aiming at improving the information obtained
273 from field monitoring, has been generated. This dataset has been obtained by
274 means of the physically based mathematical model described hereinafter (section
275 2.2.2). The model has been run with a 1000 years synthetic hourly rainfall series,
276 obtained with a stochastic rainfall generator, for which further details are given
277 in section 2.2.1.

278 **2.2.1. Definition of synthetic rainfall events**

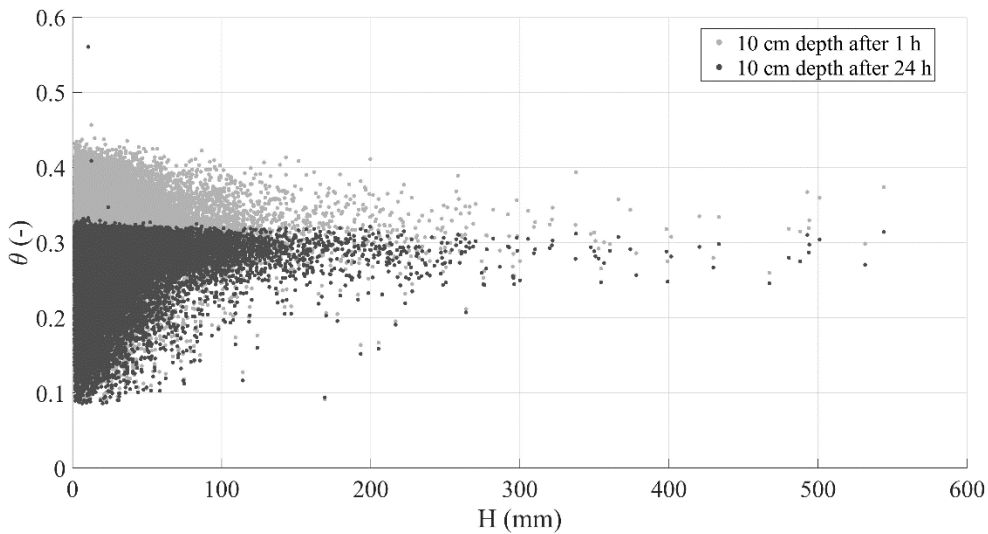
279 The Neyman-Scott rectangular pulse model (NSRP) has been used to obtain a
280 1000 years long synthetic hourly series of precipitation. The NSRP model
281 reproduces the precipitation process as a set of rain clusters, composed by

282 possibly overlapping rain cells embodied by rectangular pulses, each one with
283 random origin. The storm duration is represented by the cell width and its height
284 represents the associated rainfall intensity, so that when multiple cells overlap,
285 the total intensity is the sum of the intensities of the overlapping cells (Rodriguez-
286 Iturbe et al. 1987; Cowpertwait et al. 1996).

287 NSRP model calibration requires the identification of five parameters, using the
288 method of moments (Peres and Cancelliere, 2014), based on available rainfall
289 data for the investigated site. Specifically, the data from the rain gauge station of
290 Cervinara, situated near the Loffredo village, belonging to the Civil Protection
291 Agency of Campania Region available from January 2001 to December 2017
292 with a time resolution of 10 min, were used.

293 The aim of this study is the identification of variables expressing the slope
294 conditions responsible of different responses to precipitation. In that sense, it is
295 important to define the events within the rainfall time series to clearly distinguish
296 antecedent conditions from the effects of the current rainfall event.

297 In other words, within the 1000 years long time series, a criterion should be
298 identified to separate rainfall events, so that a new event begins only when the
299 effects of the previous one disappeared. For this study, the events were defined
300 as periods with at least 2mm of rainfall, preceded and followed by at least 24h
301 with less than 2mm (i.e., smaller than the mean daily potential evapotranspiration
302 estimated for the case study). Indeed, the separation period of 24 hours is
303 commonly used for the definition of the empirical thresholds for early warning
304 systems against rainfall-induced landslides (e.g., Peres et al., 2018; Segoni et al.,
305 2018, Marino et al., 2020b).



306
 307 **Figure 4. Scatter plot of event rainfall depth and mean volumetric water content of**
 308 **the top 10 cm soil depth 1 hour (grey dots) and 24 hours (black dots) after the end**
 309 **of each rainfall event**

310 In fact, the mean volumetric water content (θ) at 10 cm depth drops below soil
 311 field capacity ($\theta \cong 0.35$) 24 hours after the end of each event (Figure 4) in all
 312 the cases in which such value was overcome before the end of the event. This
 313 shows that a dry interval of 24 hours after a rainfall event is long enough for
 314 drainage processes to remove from the topsoil most of the water infiltrated from
 315 the previous event. As topsoil moisture controls the infiltration capacity at ground
 316 surface, after such interval the infiltration of new rainfall is only little affected by
 317 the remnants of the previous rainfall event.

318 With the assumed separation criterion, a total of 53061 rainfall events within
 319 1000 years are obtained, with durations ranging between 1 and 570 hours, and
 320 total rainfall depth between 2 and 710 mm.

321 2.2.2. Slope hydrological model

322 As already pointed out in Section 2.1, the regular geometry of the slope, and the
 323 hydraulic characteristics of the soils, make the flow processes in the soil mantle
 324 mostly one-dimensional. Indeed, a simplified 1-D model had been previously
 325 developed and successfully validated according to the data collected during the

326 hydrological monitoring activities (Greco et al., 2013; Greco et al., 2018), and
327 was applied to investigate the hydrological response of the slope to synthetic
328 hourly precipitation data. The unsaturated flow through the soil mantle is
329 modelled with 1-D head-based Richards' equation (Richards, 1931), assuming
330 for simplicity a single homogeneous soil layer, and it is coupled with a model of
331 the saturated water accumulated in the perched aquifer. The adoption of a 1-D
332 model is allowed thanks to the geometry of the considered mantle, as well as to
333 the prevailing water potential gradients orthogonal to the ground surface when
334 the soil is in unsaturated conditions.

335 The root water uptake has been accounted in the source term of the model,
336 according to the expressions by Feddes et al. (1976), based on estimated potential
337 evapotranspiration, with maximum root penetration depth equal to the soil mantle
338 thickness and triangular root density shape.

339 Two boundary conditions are considered for the unsaturated soil mantle. At
340 ground surface (i.e., the upper boundary condition), if the rainfall intensity is
341 greater than the current infiltration capacity, the excess rainfall forms overland
342 runoff. Otherwise, all rainfall intensity is set as infiltration. The bottom boundary
343 condition links the soil mantle to a perched aquifer developing in the fractures
344 and hydraulically connected to the unsaturated cover through the weathered soil
345 layer (less conductive and capable of retaining much water), located at the contact
346 between the cover and the bedrock. This soil layer penetrates the vertical conduits
347 and fractures (Greco et al., 2013). In this context, the perched aquifer is modelled
348 as a linear reservoir model, that receives water from the gravitational leakage of
349 the overlying unsaturated soil mantle and releases it as deep groundwater
350 recharge and spring discharge (Greco et al., 2018). This conceptualization of the
351 perched aquifer behaviour implies that the streamflow, supplied by the springs,
352 is linearly related to the aquifer water level temporarily developing in the
353 epikarst. Indeed, with this assumption, the model closely reproduces the trend of

354 the stream water level observed in the field (Greco et al., 2018; Marino et al.,
 355 2020a). The pressure head at the soil–bedrock interface is assumed to follow the
 356 fluctuations of the water table of the underlying aquifer.

357 The hydraulic parameters of the soil have been obtained from previous laboratory
 358 tests (Damiano and Olivares, 2010) and field monitoring data analysis (Greco et
 359 al., 2013), considering the van Genuchten-Mualem model for the hydraulic
 360 characteristic curves (van Genuchten, 1980). The parameters describing the
 361 hydraulic behaviour of the perched aquifer hosted in the upper part of the
 362 limestone bedrock have been derived from previous studies, which showed that
 363 the model satisfactorily reproduced the fluctuations of water potential and
 364 moisture, observed at various depths in the unsaturated soil cover, both during
 365 rainy and dry seasons (Greco et al., 2013; 2018). Model parameters are
 366 summarized in Table 1. The groundwater level of the perched aquifer is referred
 367 to the base of the epikarst, which is assumed 14 m below the soil-bedrock
 368 interface.

369 **Table 1. Hydraulic parameters of the coupled model of the unsaturated soil mantle**
 370 **and of the aquifer hosted in the epikarst** (Greco et al. 2021).

Soil mantle	Soil mantle thickness (m)	2
	Saturated water content (-)	0.75
	Residual water content (-)	0.01
	Air entry value (m^{-1})	6
	Shape parameter (-)	1.3
	Saturated hydraulic conductivity (m/s)	3×10^{-5}
Epikarst	Epikarst thickness (m)	14
	Effective porosity (-)	0.005
	Time constant of linear reservoir (days)	871 days

371
 372 The equations have been numerically integrated with the finite difference
 373 technique, with a time step of 1 hour over a spatial grid with vertical spacing of
 374 0.02 m.

375 It is important to note that, even if the model simplifies the reality assuming a
376 homogeneous soil profile, a more complex approach considering a layered profile
377 would lead to difficult application of the model at less detailed scales such as
378 regional and catchment scales. Consequently, the hydraulic properties of the
379 homogeneous soil layer should be considered as effective properties, useful to
380 reliably reproduce the observed phenomena.

381 **2.2.3. Synthetic hydrometeorological data**

382 As it has been stated from previous sections, the dataset comes from the
383 simulation of the hydrologic response of a slope to 1000 years long hourly rainfall
384 time series, carried out with a physically based model, calibrated for the case
385 study. The output contains the time series of soil water content and suction at all
386 depths throughout the soil mantle, of the water exchanged between the soil and
387 the atmosphere, of the leakage through the soil-bedrock interface, and of the
388 predicted water level of the underlying aquifer.

389 One hour before the onset of each rainfall event, the following variables have
390 been extracted, as they would be measurable in the field and are representative
391 of antecedent conditions: the aquifer water level (h_a), the mean volumetric water
392 content in the uppermost 6 cm of soil mantle (θ_6) and the mean volumetric water
393 content in the uppermost 100 cm of soil mantle (θ_{100}). To quantify the effects of
394 rainfall on the slope response, the change of the water stored in the soil mantle at
395 the end of each rainfall event (ΔS) has been computed and compared with the
396 total rainfall depth of the event (H).

397 Specifically, the inclusion of soil water content information has been chosen, as
398 it can be obtained from available satellite-derived remote sensing products
399 (Paulik et al., 2014; Pan et al., 2020) or from field sensor networks (Wicki et al.,
400 2020). Regarding satellite products, in many cases not giving precise water

401 content values, they satisfactorily reproduce temporal trends, which represent a
402 valuable information for hazard assessment.

403 Besides, as the model introduces a linear relationship to estimate the outflow
404 from the groundwater system, the monitored stream water level has been
405 considered comparable to the simulated groundwater level, as the two variables
406 are assumed directly proportional in the model.

407 **2.3. Data analysis techniques**

408 The resulting dataset has been analyzed with Machine Learning techniques,
409 aiming at capturing the complex interactions between the hydrological
410 subsystems (i.e., soil mantle, fractured bedrock, surface water). Indeed, the
411 analysis of the data is not only constrained to classical statistical analyses, such
412 as data frequency distributions, but also to data classification based on their
413 geometrical distribution, and on quantifying the importance of the considered
414 antecedent variables on the simulated response as well.

415 **2.3.1. Variable importance assessment by Random Forest**

416 The Random Forest is a Machine Learning method that sets its basis on the theory
417 of regression/classification trees, bagging data and capturing even the complex
418 or non-linear interactions in-between the data of a set with relatively low bias
419 (Breiman, 2001). This method is often used to forecast a desired variable based
420 on predictor variables in terms of regression or classification set of randomly
421 constructed trees. In this case, a regression based Random Forest technique is
422 applied to predict the soil storage response (ΔS) at the end of each rainfall event
423 of total depth H , using as predictors all possible triplets of variables described in
424 the section 2.2.3 (H , h_a , θ_6 and θ_{100}). Specifically, four Random Forest models
425 have been developed: RF1 with input features $\langle H, \theta_6, h_a \rangle$, RF2, with input
426 features $\langle H, \theta_{100}, h_a \rangle$, RF3, with as input features $\langle H, \theta_6, \theta_{100} \rangle$ and RF4 with input
427 features: $\langle H, \theta_6, \theta_{100} \rangle$. The 80% of the dataset was used to train the models and

428 tuning the major hyperparameters of random forest algorithm: the number of
429 trees, the maximum depth, the minimum sample leaf, and the maximum number
430 of feature (more details about the evaluation and optimization of the
431 hyperparameters are provided in Appendix B).

432 Then, the best predictor triplet of variables is selected according to the lowest
433 value of the Root Mean Squared Error (RMSE) calculated using the test data set
434 consisting of the 20% of the remaining data.

435 Furthermore, to understand how a single variable affects the regression model,
436 the predictor importance is measured by the sensitivity of Random Forest model
437 to the predicted variable (i.e., soil mantle response), which is proportional to the
438 RMSE, by permuting on purpose the variables between the levels of the model
439 and calculating the corresponding change in the RMSE. Hence the most
440 important variable is the one that exhibits the greatest change in RMSE after the
441 permutations (Hastie et al., 2008).

442 **2.3.2. Data classification by clustering analysis**

443 The exploratory analysis of spatial large datasets is often performed by means of
444 clustering techniques, aiming at identifying different classes in the data,
445 accounting on the distribution of the variables under study. There are two types
446 of clustering algorithms used for class identification purposes: algorithms based
447 on the density of points and algorithms based on the distance between points. The
448 algorithm used here is named k-means, and it is a distance-based procedure to
449 cluster data, based on the number of desired clusters and their centroids. The
450 algorithm assigns every element in the dataset to a cluster, iteratively minimizing
451 the variance of the Euclidean distance of the elements of each cluster from their
452 centroids. Consequently, the data labelling is done based on their geometrical
453 disposition in the dot cloud, depending on the target number of clusters to be
454 identified (Lloyd, 1982; Arthur and Vassilvitskii, 2007). When variables with

455 very different magnitudes are being related for clustering purposes, it is
456 convenient to normalize the data keeping the relative distances between
457 observations. Therefore, the clustering here is applied to the standardized data to
458 exploit the variance of each variable and keeping the geometrical disposition
459 between observations stable.

460 As the k-means algorithm does not automatically estimate the optimal number of
461 clusters to be identified within the dataset, the Silhouette metric has been used
462 here to evaluate the preferred number of clusters (Rousseeuw, 1987; de Amorim
463 and Hennig, 2015). In fact, this metric quantifies the quality of cluster
464 identification by scoring the difference between the overall average intra-cluster
465 distances and the average inter-cluster distances related to the maximum between
466 the latter two. In that way the metric would always be a value ranging from -1
467 and 1, where typically 1 means that clearly distinguished clusters have been
468 identified, 0 means that the identified clusters are indifferent, and -1 means that
469 data are mixed in the identified clusters.

470 **3. Results and discussion**

471 The analysis is carried out on both field monitored and synthetic datasets, to
472 quantify the information provided by the defined antecedent variables useful to
473 predict the seasonal changes of the slope response to precipitation.

474 **3.1. Role of measurable variables on the response of the soil mantle**

475 To select the most informative triplets of variables, for predicting the change in
476 water storage (ΔS) in the soil mantle, associated to rainfall events of total depth
477 H , four Random Forest models are trained to predict the ratio $\Delta S/H$, based on the
478 dataset consisting of all possible combinations of the synthetic variables:
479 $\langle H, \theta_6, h_a \rangle$, $\langle H, \theta_{100}, h_a \rangle$, $\langle H, \theta_6, \theta_{100} \rangle$ and $\langle \theta_6, \theta_{100}, h_a \rangle$. In fact, the change in
480 storage ΔS is obviously strongly dependent on the event rainfall depth H (i.e., the
481 more it rains the more soil storage increases), thus concealing important

482 hydrological processes going on the slope. Differently, the choice of the ratio
 483 $\Delta S/H$, a measure of the amount of rain that remains stored in the soil mantle,
 484 allows detaching the water drainage processes from the water accumulation
 485 processes. For each Random Forest model, the values of the Root Mean Square
 486 Error (RMSE) are calculated, and the importance of each predictor variable is
 487 evaluated according to the procedure described in Section 2.3.1. The
 488 computational effort implied in doing the calculations by a conventional
 489 workstation with a Core(TM) i7-10870H processor and 16 GB of SDRAM
 490 memory is less than 2 minutes for each model run. The obtained results are
 491 reported in Table 2.

492 **Table 2. RMSE and variable importance for H , θ_6 , θ_{100} and h_a in the prediction of**
 493 **soil response described as $\Delta S/H$**

Dataset	RMSE	Importance			
		H	θ_6	θ_{100}	h_a
$\langle H, \theta_6, h_a \rangle$	0.213	0.352	0.329	-	0.319
$\langle H, \theta_{100}, h_a \rangle$	0.197	0.293	-	0.405	0.302
$\langle H, \theta_6, \theta_{100} \rangle$	0.203	0.340	0.261	0.399	-
$\langle \theta_6, \theta_{100}, h_a \rangle$	0.210	-	0.292	0.414	0.293

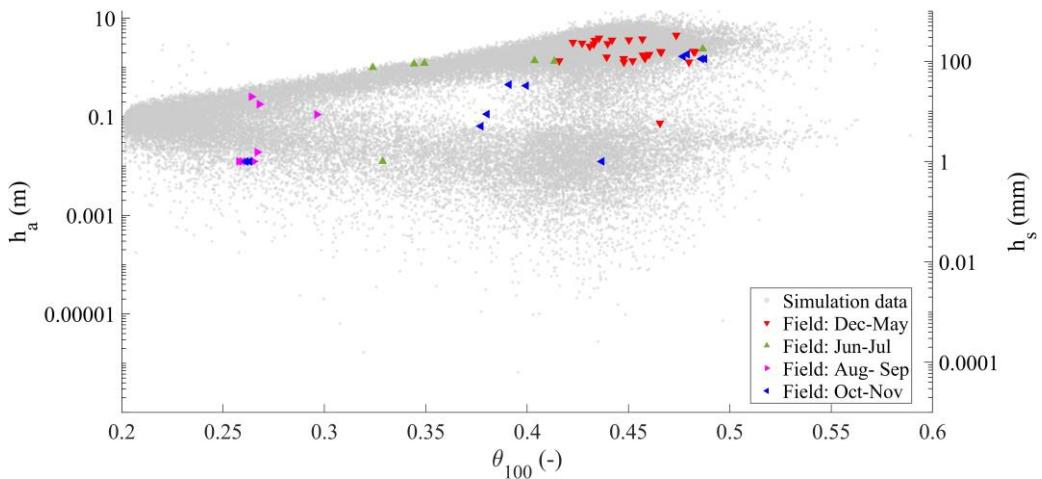
494

495 All the choices of triplets indicate that all the tested variables are similarly
 496 informative to predict the normalized soil mantle response $\Delta S/H$ (Table 2). It is
 497 worth to note the importance of the perched ground water level, which can be
 498 compared with the importance of the soil water content and of the total rainfall
 499 depth. The importance of h_a on the response of the soil mantle suggests that, in
 500 some conditions, the change in soil storage is affected by the effectiveness of
 501 water exchange between the soil mantle and the underlying aquifer, as it will be
 502 discussed in the following sections. Moreover, in Table 2 the triplet showing the
 503 lowest RMSE values is conformed by the total rainfall depth, the aquifer water

504 level and the mean volumetric water content in the uppermost 100 cm. According
505 to the Random Forest model, they are the most informative for predicting the soil
506 mantle response. Therefore, the triplet $\langle H, \theta_{100}, h_a \rangle$ is used for further analysis.

507 3.2. Soil and underground antecedent conditions

508 The field monitoring activities allow to get a complete dataset that traces the
509 rainfall values coupled with the soil mean volumetric water content in the
510 uppermost meter of the soil profile (θ_{100}) and the water depth of the Castello
511 stream (h_s), both measured hourly for three years. The field monitored data,
512 composed by 57 rainfall events, include the water level of the Castello stream
513 rather than the direct measurement of the aquifer water level (h_a). Nevertheless,
514 a direct relationship links the water level in the aquifer and the water level in the
515 stream, as assumed for the mathematical modelling. This dataset has been
516 enriched synthetically, as it has been described in section 2.2.

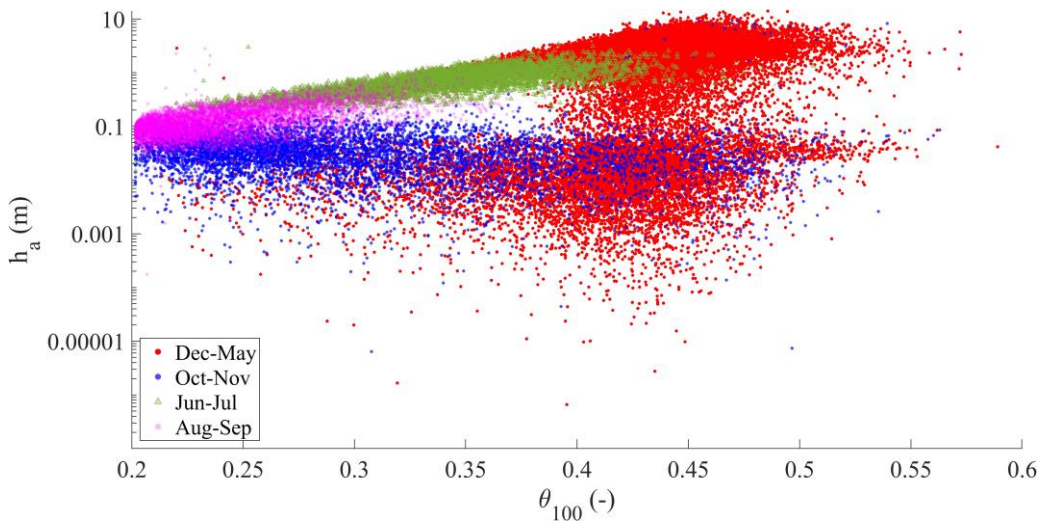


517
518 **Figure 5. Field monitored mean volumetric water content in the upper meter of the**
519 **soil profile (θ_{100}) and water depth in the Castello stream (h_s) compared with**
520 **simulated data (the vertical axis is plotted in logarithmic scale to help visualizing of**
521 **small water levels).**

522 Therefore, to analyze the effects of the underground conditions on the slope
523 response, Figure 5 shows the simulated data (circular dots in the background) and

524 the field monitored data (triangular colored dots). Logarithmic axes are used to
525 distinguish the very low aquifer water level from the high values.

526 Four major seasonally recurrent conditions could be identified for the water in
527 the subsurface system from field monitored data: first, a condition usually
528 occurring between December and May is characterized by the highest water
529 content in the soil and the highest measured water level in the stream. Second,
530 the period from June to July is characterized by intermediate water content
531 values, with still high level in the stream. Third, the period from August to
532 September is characterized by the lowest values of water content in the soil, but
533 also the lowest water depth h_s measured in the stream (few centimeters, in some
534 cases nearly zero). Finally, the period from October to November is characterized
535 by a wide range of values in soil water content and a relatively low range of
536 stream water depth.

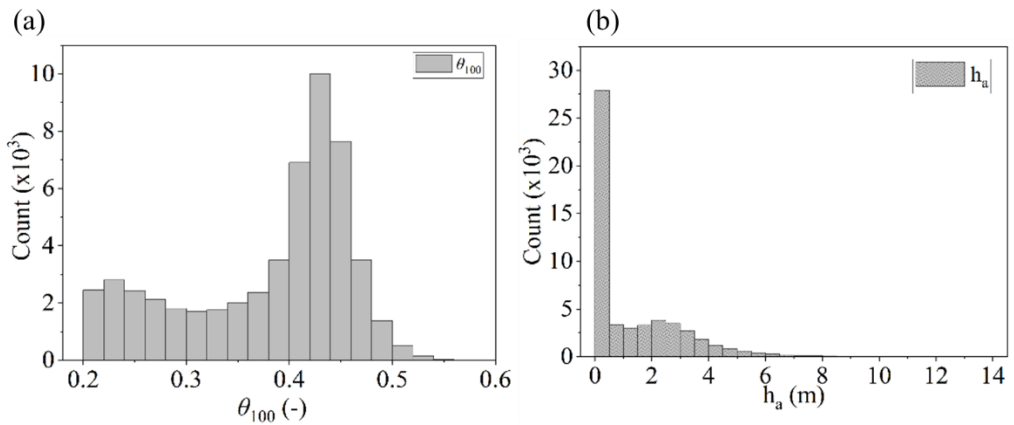


537
538 **Figure 6. Seasonal behavior of the aquifer water level (h_a) and the mean**
539 **volumetric water content of the upper meter of the soil profile (θ_{100}) for the**
540 **synthetic dataset (the vertical axis is plotted in logarithmic scale to help**
541 **visualizing small water levels).**

542 The underground antecedent conditions are naturally linked to a seasonal
543 behavior dominated by the hydrological conditions which can be traced in time

544 as it can be seen from the synthetic data (Figure 6). The months from December
 545 to April follow a winter and spring behavior, characterized by wet soil conditions
 546 and aquifer water levels ranging from low to high. From June to July, a late spring
 547 behavior is visible, characterized by relatively dry soil (i.e., most of the data
 548 falling below soil field capacity), in combination with relatively high
 549 groundwater levels (indicating a still active slope drainage). In August and
 550 September, a summer like behavior is shown, with the driest soil water content
 551 and generally low aquifer water level. Finally, in October and November, the end
 552 of the dry season is shown: a wide range of soil wetness coupled with a still low
 553 aquifer water level.

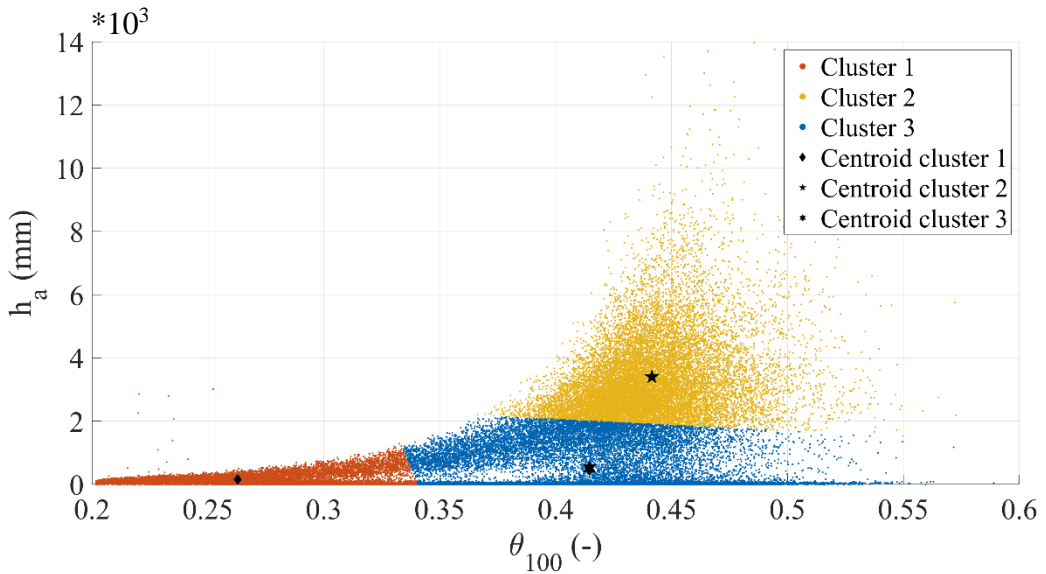
554 For both the field monitored and synthetically obtained datasets, the observed
 555 conditions are the result of the time lag between the beginning of the rainy season
 556 and the slope response. The recurrent seasonal behavior observed for the
 557 synthetic dataset, although delayed or anticipated owing to the year-by-year
 558 variability of rainfall, is close to that observed in the field.



559
 560 **Figure 7. Histograms for data distributions of (a) θ_{100} and (b) h_a for the synthetic**
 561 **dataset**

562 The overall situation for the synthetic dataset of antecedent conditions (i.e.,
 563 duplets $\langle \theta_{100}, h_a \rangle$) can be described by the distribution of each individual
 564 variable, which can be seen in the histograms shown in Figure 7. It is interesting

565 to note that, for both θ and h_a , a bimodal behaviour is observed, corresponding
566 to dry and wet field conditions.

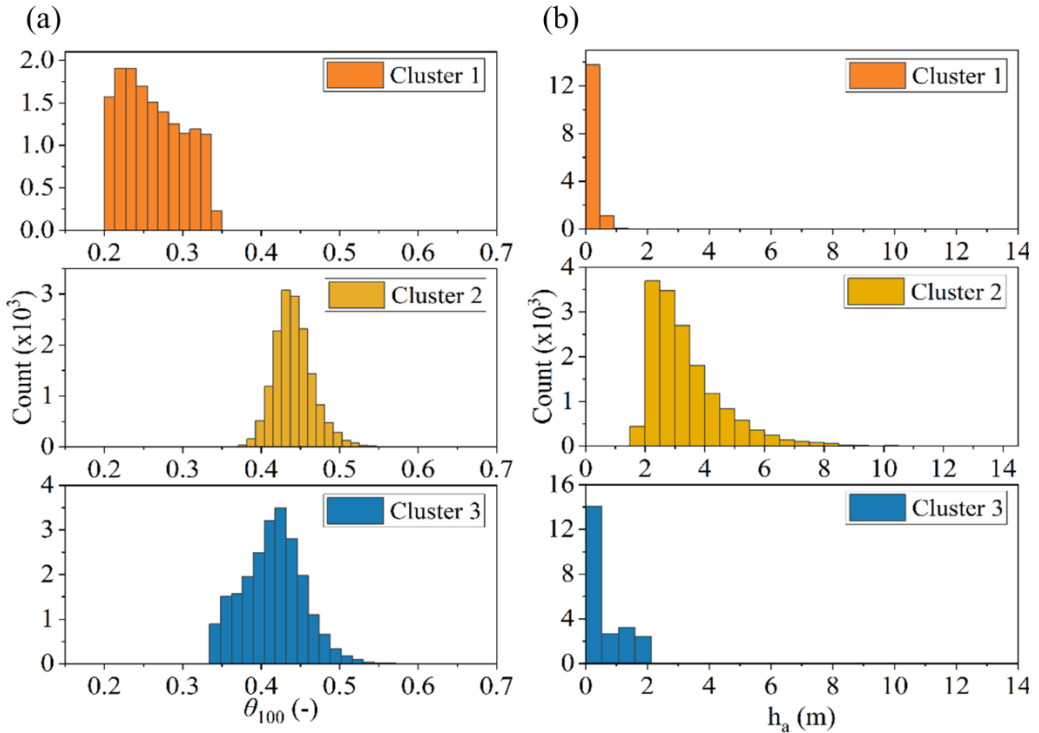


567

568 **Figure 8. Identified clusters for the duplets $\langle \theta_{100}, h_a \rangle$ representing underground**
569 **antecedent conditions of the synthetic dataset. For each cluster, the centroids are**
570 **shown.**

571 The k-means clustering technique has been used to investigate the geometrical
572 distribution of the duplets $\langle \theta_{100}, h_a \rangle$, with number of clusters ranging from 2 to
573 7. According to the Silhouette metric, the optimal number of clusters is 3, with a
574 metric value of 0.7, allocating the 28%, 30% and 42% of the data in clusters 1, 2
575 and 3 respectively. Figure 8 shows the 3 clusters obtained within the synthetic
576 dataset. Centroid positions are also displayed, showing the zones of the clouds
577 where most of the dots are gathered. This representation of the data use both
578 vertical and horizontal axes in linear scale to let visualize distance magnitudes
579 between the different clusters, but it corresponds to the same dataset shown in
580 Figure 6.

581 The distribution of the data after clustering is also analyzed for each cluster and
 582 the histograms are shown in Figure 9. It looks clear that the clusters capture
 583 different couplings of dry and wet underground antecedent conditions.



584
 585 **Figure 9. Histograms for data distributions of (a) θ_{100} and (b) h_a , according to**
 586 **each identified cluster in the duplets $\langle \theta_{100}, h_a \rangle$**

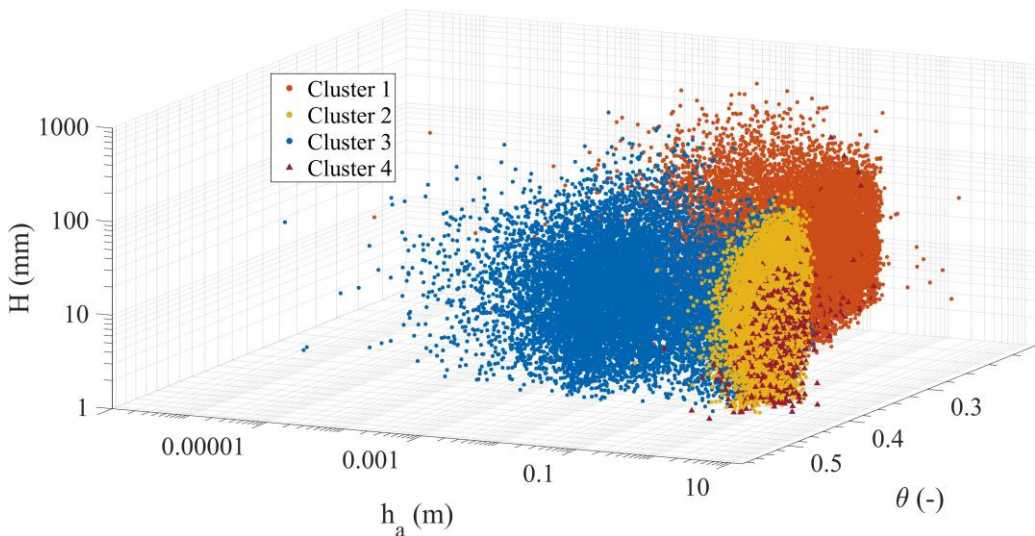
587 In fact, cluster 1 captures dry conditions, with a volumetric water content below
 588 the field capacity θ_{fc} (it was estimated as 0.35 with the empirical relationship
 589 proposed by Twarakavi et al. (2009) according to the van Genuchten model
 590 parameters) and low values of h_a . Differently, clusters 2 and 3 capture scenarios
 591 related to relatively wet soil mantle conditions (i.e., $\theta_{100} > \theta_{fc}$), coupled to low
 592 h_a in cluster 3, gathering scenarios normally observed in late autumn, and to the
 593 highest h_a conditions for cluster 2, comprising conditions normally occurring in
 594 late winter and spring.

595 The two chosen variables, θ_{100} and h_a , allow identifying three different
596 antecedent slope conditions one hour before the onset of any rainfall event.
597 Hence, it is worthy to investigate how these different antecedent conditions may
598 be related to different slope responses to precipitation.

599 **3.3. Effects of soil and underground antecedent conditions on the**
600 **slope response to rainfall**

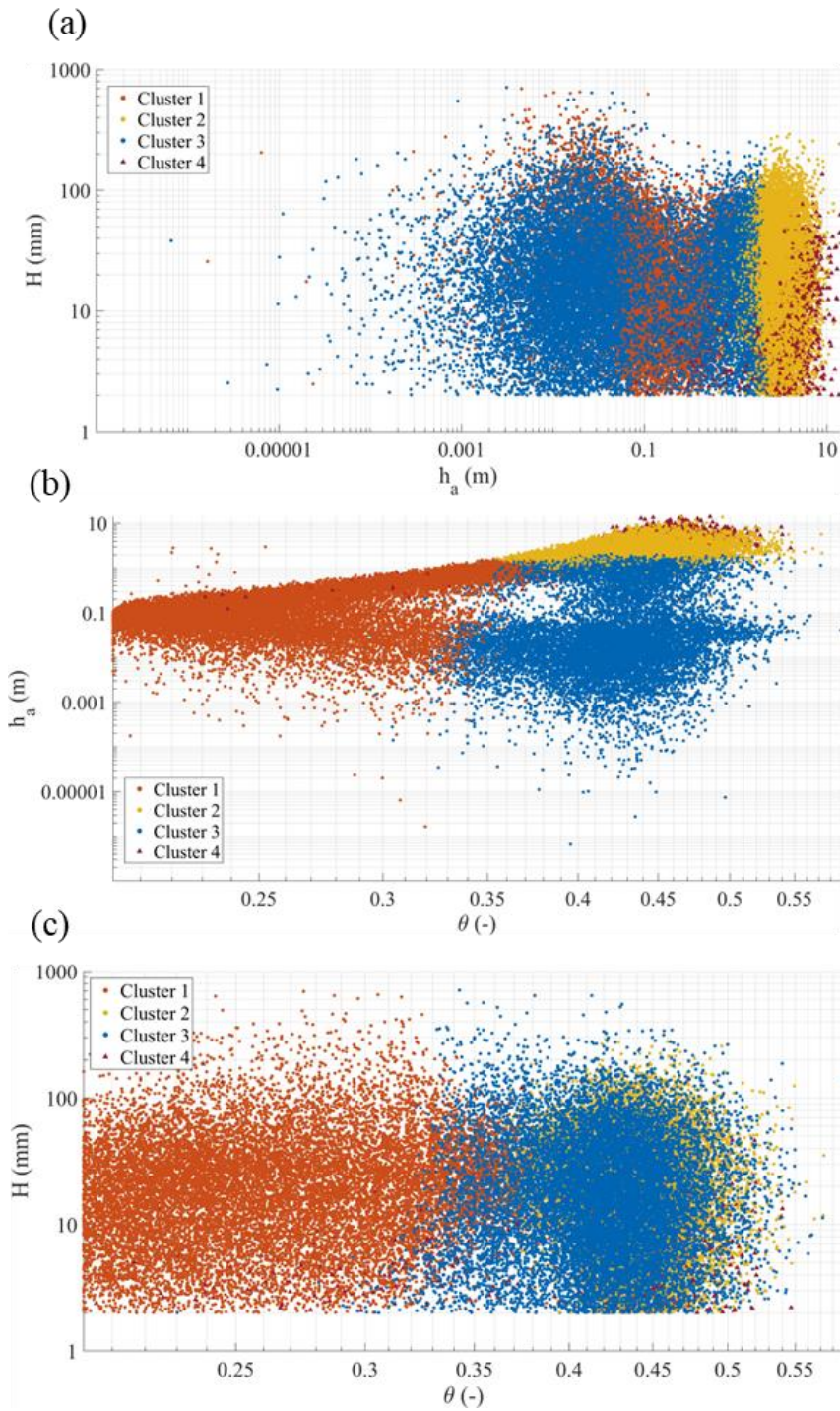
601 The analysis of the data has been focused on identifying clusters within the
602 triplets $\langle \theta_{100}, h_a, \Delta S/H \rangle$, aiming to evaluate the slope response as the amount of
603 rainwater being stored/drained in the soil mantle. The results are being plotted in
604 the space composed by the variables that can be monitored in the field:
605 (θ_{100}, h_a, H) .

606 As it is not always expected to experience increased soil storage during rainfall
607 events, the identification of draining slope conditions is an important aspect.



608
609 **Figure 10. Clustering results of the synthetic data triplets $\langle \theta_{100}, h_a, \Delta S/H \rangle$**
610 **represented in the space (θ_{100}, h_a, H)**

611



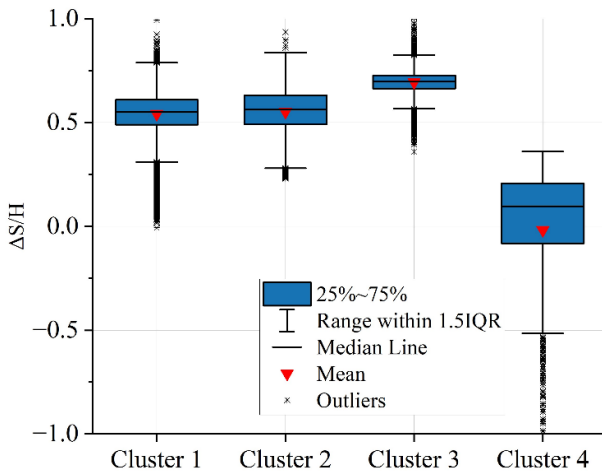
612

613

614

Figure 11. Clustering results of the triplets $\langle \theta_{100}, h_a, \Delta S/H \rangle$ in (a) (θ_{100}, h_a) plane; (b) (θ_{100}, H) plane; (c) (H, h_a) plane

615 Figure 10 and Figure 11 show the data clusters for the triplets $\langle \theta_{100}, h_a, \Delta S/H \rangle$,
 616 for any identified rainfall event, represented in the (θ_{100}, h_a, H) space in a
 617 logarithmic axis representation. The Silhouette metric in this case suggests 4 as
 618 an optimal number of clusters with a metric value of 0.61. It is remarkable that
 619 three of the clusters are close to those already identified from the antecedent
 620 (seasonally recurrent) underground conditions (section 3.2).



621
 622 **Figure 12. Distribution of the slope response $\Delta S/H$ for the data in each cluster**

623 Specifically, cluster 1, 2 and 3 correspond to different slope processes according
 624 to $\Delta S/H$ (Figure 12). Even if cluster 1 and cluster 2 show similar responses, with
 625 slightly smaller $\Delta S/H$ for cluster 1, the controlling processes are indeed different;
 626 the conditions of cluster 1 are typically occurring in dry seasons with long dry
 627 periods between short rainfall events, leading to dry antecedent conditions, so
 628 that accumulation of water in the soil mantle (increase in water storage) is
 629 expected at each event. The data in cluster 2 are typically related to wet seasons,
 630 especially in late winter and spring, where rainfall events are more frequent,
 631 leading to antecedent wet soil ($\theta_{100} \geq \theta_{fc}$) and antecedent high ground water
 632 level. However, these conditions do not seem to correspond to effective slope
 633 drainage, so that the slope response in cluster 2 results comparable to that
 634 observed in cluster 1 in terms of $\Delta S/H$. Instead, the conditions gathered in cluster

635 3 differ from those in cluster 2 for the lower aquifer water level h_a , and the
636 highest $\Delta S/H$ indicates the lowest slope drainage.

637 The additional cluster 4 identified here highlights a particular slope response, as
638 it catches all the conditions where nearly zero and negative ΔS take place,
639 meaning an effective slope drainage during rainfall events. It is interesting to note
640 that, even for relatively high rainfall events (above 100 mm), this slope response
641 occurs when soil moisture is above the field capacity and when this condition is
642 coupled with very high groundwater level, probably due to the high permeability
643 all along the soil mantle and to the hydraulic connection with the underlying
644 aquifer.

645 **4. Conclusions**

646 This study aims at identifying and analysing the major hydrological controls of
647 the slope response to precipitation and, in that way, defining suitable variables to
648 be monitored in the field to predict such response. The studied case refers to the
649 hydrological processes in a slope system consisting of a pyroclastic soil mantle
650 overlaying a fractured karstic bedrock, where a perched aquifer develops during
651 the rainy season. A synthetic time series of slope response to precipitation has
652 been built, thanks to a physically based model, previously calibrated with field
653 monitoring data, coupled with a stochastic rainfall generator. Synthetic and
654 experimental data show substantial agreement. In fact, the soil water content
655 values measured in the field are close to those of the synthetic dataset.
656 Furthermore, the simulated epikarst water level shows similar seasonal behaviour
657 as the stream level records, indeed directly related with the discharge from the
658 epikarst aquifer. The synthetic dataset has been explored with Random Forest
659 and k-means clustering, to evaluate the slope response characterized as the
660 change in water stored in the soil mantle (ΔS) during precipitation events with
661 rainfall depth H , starting from different underground antecedent conditions.
662 These were quantified through the mean volumetric water content in the

663 uppermost meter of soil mantle (θ_{100}) and the aquifer water level (h_a), one hour
664 before the onset of rainfall.

665 The ratio $\Delta S/H$, which allows identifying slope response regardless the amount
666 of event precipitation, is sensitive to both h_a and θ_{100} , with the groundwater level
667 being the most influential antecedent variable. The underground antecedent
668 conditions, characterized by θ_{100} and h_a and linked to the seasonal
669 meteorological forcing, allow identifying different slope responses, related to the
670 seasonally active hydrological processes.

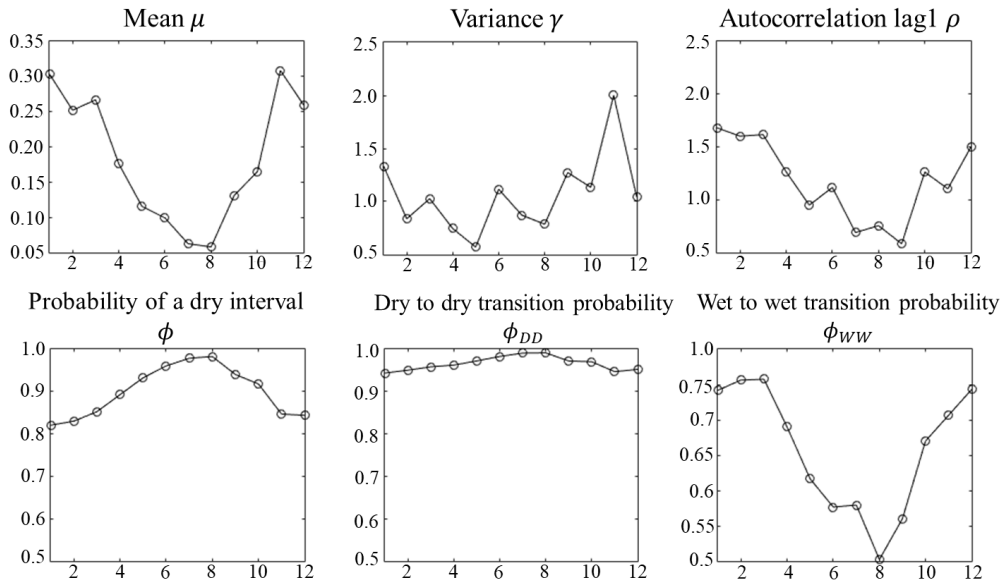
671 High perched groundwater level, typical of winter and spring, indicates active
672 slope drainage, which compensates rainwater infiltration, so that the soil storage
673 remains stable, or even reduces, even after large rainfall events.

674 Differently, low perched groundwater level corresponds to impeded slope
675 drainage. When it occurs with initially dry soil mantle (typically in summer and
676 early autumn), it tends to retain all the infiltrated rainwater as increased soil
677 storage. When the soil mantle is already wet (i.e., above the field capacity) at the
678 onset of rainfall events, as it usually happens in late autumn and early winter, the
679 increase of soil storage is smaller, as the soil approaches saturation.

680 The presented results suggest that monitoring antecedent conditions, by
681 measuring suitable variables to identify the major hydrological processes
682 occurring in the slope in response to precipitation, can be useful to understand
683 such processes and to develop effective predictive models of slope response.
684 Therefore, the proposed methodology can be replicated also in other contexts and
685 be useful for several hydrologic applications: from the water supply towards
686 natural streams due to infiltrated water, to the hydric stress estimation in crops
687 (e.g., the centenary chestnut forests of the case study) especially in very dry
688 seasons, but also for the design of effective monitoring networks exploiting
689 geohydrological information for geohazard prevention (and early warning).

690 **Appendix A: Calibration of the Stochastic Rainfall Generator**

691 The Neyman-Scott Rectangular Pulse (NSRP) model (Neyman and Scott, 1958;
692 Rodriguez-Iturbe et al., 1987; Cowpertwait et al., 1996) is here used as stochastic
693 rainfall generator. The NSRP describes the process of point rainfall as a
694 superposition of randomly arriving rain clusters, each containing several rain
695 cells with constant intensity. The hyetograph within a cluster is obtained by
696 summing the intensity of the various cells belonging to the cluster. It has been
697 calibrated based on 17 years of experimental data (2000-2016) of rainfall depth
698 at 10 min time resolution, recorded by the rain gauge managed by the Civil
699 Protection in Cervinara (Southern Italy). The calibration has been carried out by
700 minimizing, for rainfall aggregated at various durations, the difference between
701 the following quantities, estimated by the model and calculated from the
702 experimental data: mean, variance, lag 1 autocorrelation, probability of dry
703 interval, probability of transition from dry-to-dry interval and probability of
704 transition from wet-to-wet interval. The calibration procedure, based on the one
705 proposed by Coptwertwait et al. (1996), is described in detail in Peres and
706 Cancelliere (2014). To account for the seasonality of rainfall, these quantities
707 have been calculated month by month in the experimental record (Figure A1),
708 suggesting that the calibration of the NRSP model should be carried out
709 separately for seven homogeneous periods (September, October, November,
710 December-March, April, May-June, July-August).



711

712 **Figure A1. Monthly plot of hourly rainfall characteristics calculated based on the**
 713 **experimental data of the rain gauge of Cervinara.**

714 Table A1 gives the obtained parameters of the NSRP stochastic model, where λ
 715 represents the parameter of a Poisson process describing the arrival of clusters; ν
 716 is the mean number of cells in a cluster, also described by a Poisson process; β is
 717 the parameter of an exponential probability distribution describing the arrival
 718 times of each cell in a cluster, expressed as the number of time intervals of 10
 719 minutes starting from the beginning of a cluster; η is the parameter of an
 720 exponential probability distribution describing the duration of rain cells; ξ is the
 721 parameter of a Weibull probability distribution describing the rain intensity of
 722 cells, with cumulative probability function $F(x, \xi, b) = 1 - \exp(-\xi x^b)$, in which
 723 x is cell rain intensity and the parameter $b = 0.8$ has been set a priori
 724 (Cowpertwait et al., 1996).

725

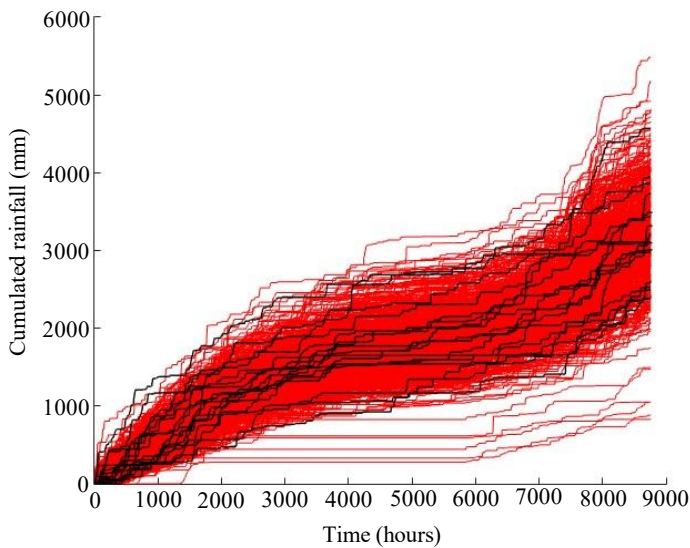
726

727

728 **Table A1. Parameters of the NSRP model.**

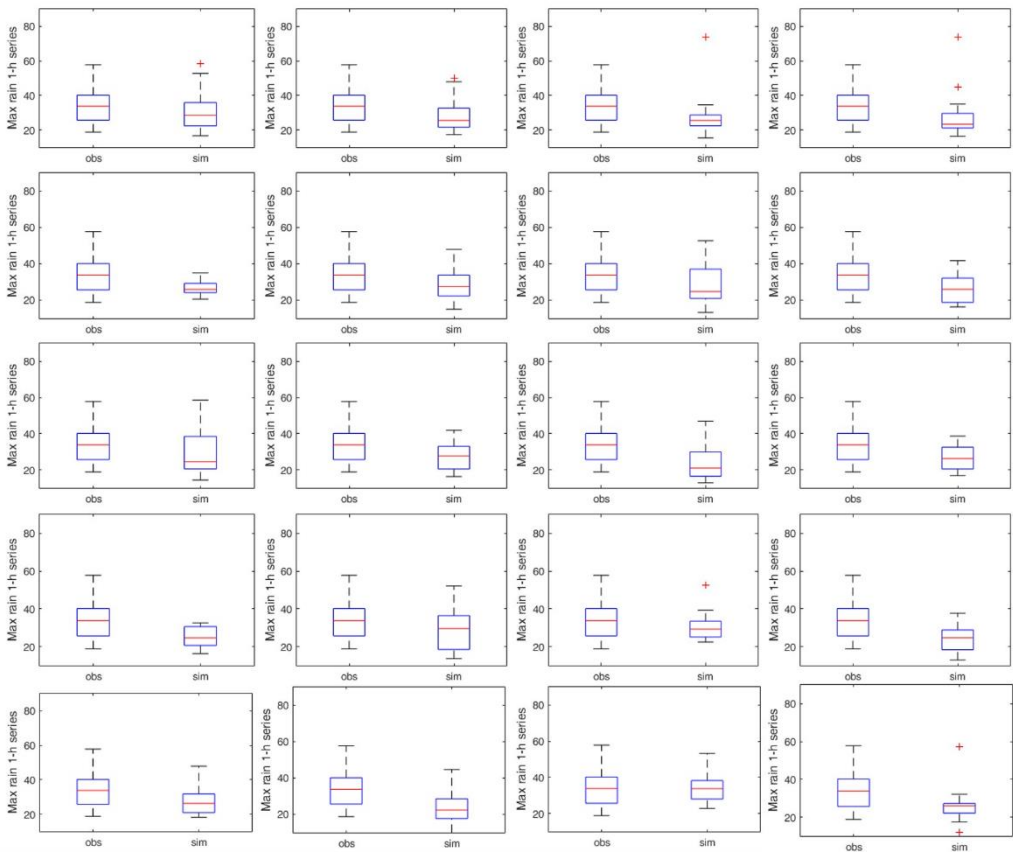
Param	Sept	Oct	Nov	Dec- Mar	Apr	May- Jun	Lug.Au g
λ (h^{-1})	0.01 5	0.0052 4	0.0025 7	0.0238	0.0080 9	0.00386	0.00900
ν (-)	2.68	36.4	57.1	2.60	38.7	21.6	1.40
β (h^{-1})	0.26 5	0.156	0.0167	0.813	0.123	0.116	24.5
η (h^{-1})	1.41	57.3	1.43	0.280	15.5	8.59	1.23
ξ (h^b mm^{-b})	0.33 0	0.047	0.450	0.967	0.186	0.158	0.268

729 The adherence of the rainfall generated with the stochastic model to the
 730 experimental rainfall data has been tested by evaluating rainfall characteristics
 731 different from those used for the calibration. For instance, Figure A2 shows the
 732 comparison of the rainfall depth, cumulated over one year, for the experimental
 733 data (17 years) and for 1000 years of synthetic data generated with the calibrated
 734 NSRP model.

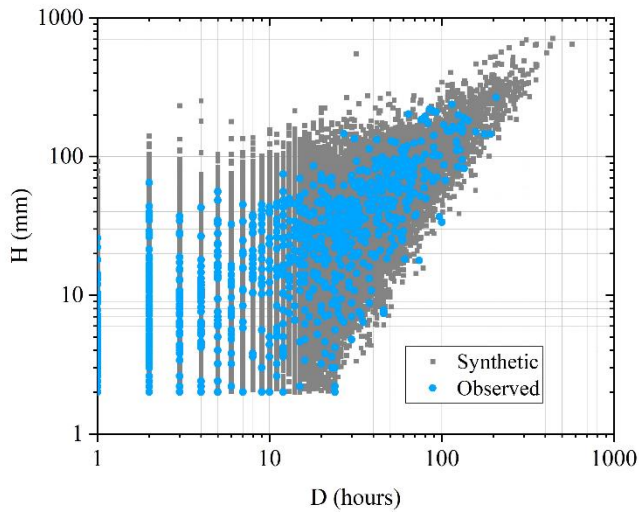


735
 736 **Figure A2. Comparison of observed (black) and simulated (red) cumulated rainfall**
 737 **plots in a year.**

738 In Figure A3, the boxplot of the maximum hourly rainfall in one year, observed
739 in the experimental dataset of 17 years, is compared with the same boxplot
740 referred to 20 series of 17 years randomly extracted from the generated 1000
741 years synthetic rainfall series. Several of the synthetic 17 years intervals show a
742 distribution of the maximum hourly rainfall close to the observed one.



743
744 **Figure A3. Comparison of observed and simulated distributions (boxplots) of the**
745 **maximum hourly precipitation in a year, for series of the same length. Each panel**
746 **shows the distribution for the 17 observed years (boxplot is always the same), and**
747 **17 randomly picked simulated years.**

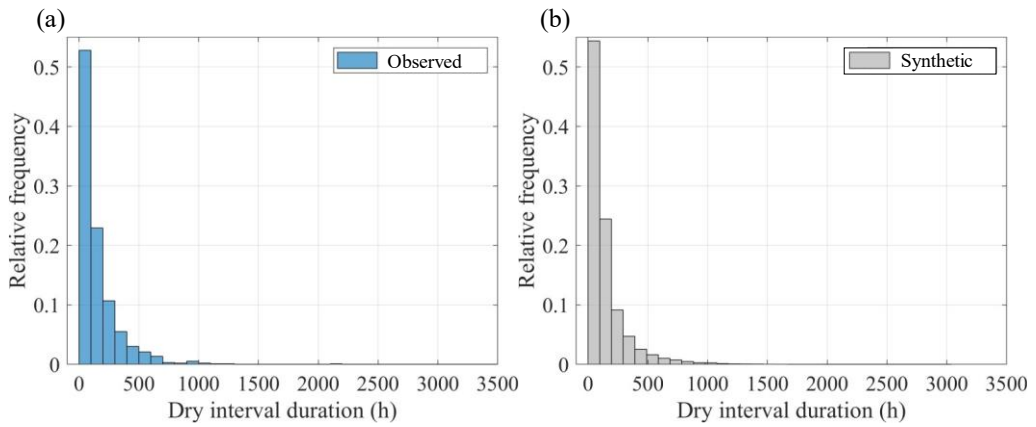


748

749 **Figure A4. Scatterplot of total rainfall event depth (H) vs. rainfall event duration**
 750 **(D). The events have been sorted within the rainfall datasets by considering a**
 751 **separation “dry” interval of 24 hours with less than 2 mm rainfall. The blue dots**
 752 **represent events extracted from the 17 years experimental rainfall dataset, while**
 753 **the grey dots represent events extracted from the 1000 years synthetic rainfall**
 754 **dataset.**

755 Regarding the required comparison between synthetic and observed wet and dry
 756 intervals, figure A4 shows the scatterplot of duration and total rain depth of the
 757 events, sorted with a separation “dry” interval of 24 hours with less than 2 mm
 758 rainfall from the observed dataset (blue dots) and the synthetic dataset (grey
 759 dots). The plots show how the synthetic data contain the observed ones, and that
 760 the shape of the dot clouds looks quite similar.

761 Figure A5 shows the frequency distributions of the durations of dry intervals
 762 belonging to the 17 years rainfall dataset, and the same distribution for the dry
 763 intervals extracted from the 1000 years synthetic dataset: the two distributions
 764 look nearly identical.



765

766 **Figure A5. Frequency distributions of dry interval durations for events extracted**
 767 **from the 17 years experimental rainfall dataset (a) and events extracted from the**
 768 **1000 years synthetic rainfall dataset (b). The events have been sorted within the**
 769 **rainfall datasets by considering a separation “dry” interval of 24 hours with less**
 770 **than 2 mm rainfall.**

771

772 **Appendix B: Tuning Random Forest hyperparameters**

773 The Random Forest (RF) algorithm (Breiman, 2001) has been very successful as
774 a general-purpose classification and regression method. Starting from Bagging
775 or Bootstrap Aggregation (Efron and Tibshirani, 1993), RF builds several random
776 de-correlated decision trees and then averages their predictions.

777 The regression RF algorithm can be summarized as follows: 1) by means of
778 bootstrap, a sample is extracted from the training data; 2) based on the
779 bootstrapped data, a tree T of the random-forest is grown by repeating the
780 following operations until a leaf node (a node without split) is reached: a) for
781 each node, m variables are randomly selected from the p input variables or
782 features (with $1 \leq m \leq p$); b) among the m variables, the best variable and
783 splitting point are selected according to a minimum criterium; c) the node is split
784 into two daughter nodes. To build the RF with B trees, steps 1 and 2 are repeated
785 B times. Then, the prediction, Y_{pred} , for a new observation, X , is the average of
786 the final values, $T_b(X)$, i.e., the values of the predicted variable corresponding to
787 the leaves of each tree:

$$788 \quad Y_{pred} = \frac{1}{B} \sum_{b=1}^B T_b(X) \quad (\text{B.1})$$

789 The main advantage of RF is the simplicity with which a forest can be trained,
790 and the parameters of the algorithms optimized. In this paper, the scikit-learn
791 framework (Pedregosa et al, 2011) is used to run the RF algorithm.

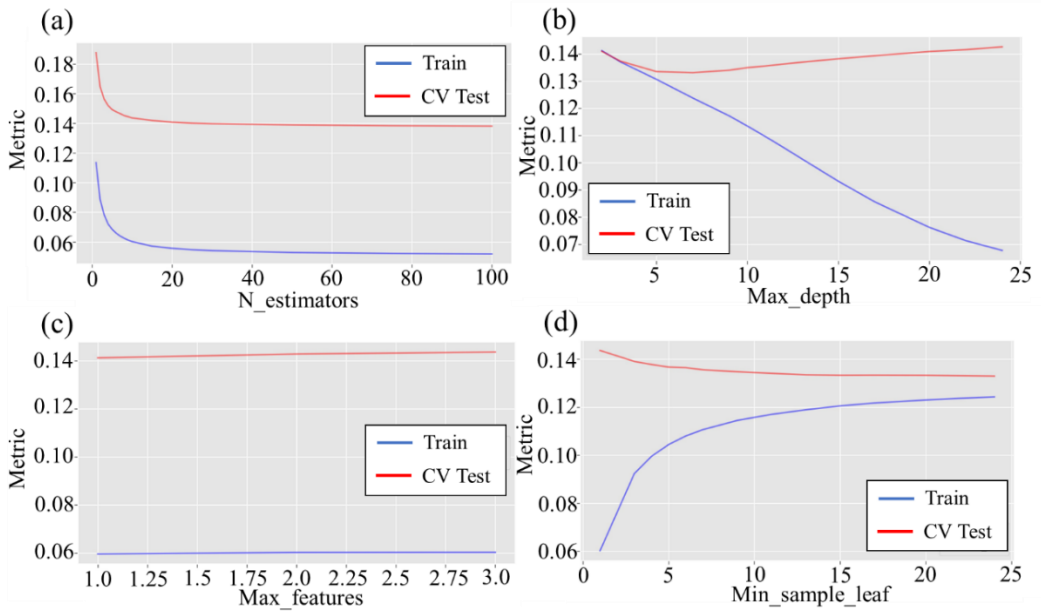
792 The main hyperparameters of a RF are: 1) `n_estimators`: the number of trees of
793 the forest; 2) `max_depth`: the maximum depth of each decision tree in the forest;
794 3) `min_samples_leaf`: the minimum number of samples required to be at a leaf
795 node; `max_features`: the number of features, or input variables, to consider when
796 looking for the best split.

797 The procedure applied in this study to estimate and optimize the hyperparameters
798 of the RF algorithm consists of the following steps:

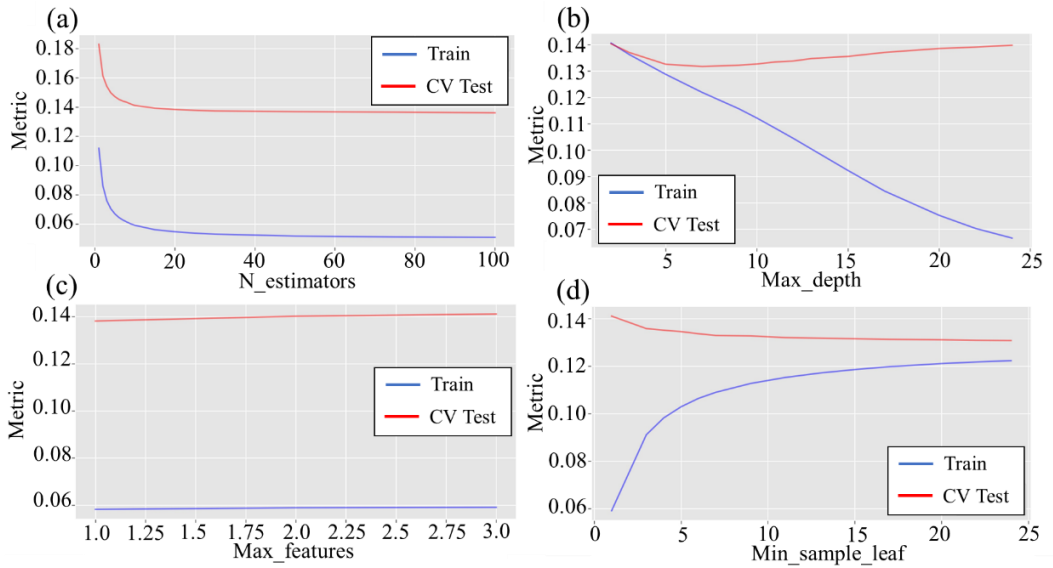
- 799 - Step 1: the dataset is divided into a training set and a test set, respectively
800 containing 80% and 20% of the data, randomly chosen.
- 801 - Step 2: the K-fold cross-validation technique (Stone, 1974), with K=10,
802 is applied to empirically determine a set of values for the
803 hyperparameters, using only the training dataset.
- 804 - Step 3: for each fold, a RF is trained on the other k-1 folds of the data and
805 tested on the first fold. This process is repeated k=10 times, so to use each of
806 the k folds exactly once as the validation set. A performance metric is then
807 calculated for each fold, to estimate how well the RF will perform on new
808 data. In this work the Root Mean Square Error (RMSE) is used as the
809 performance metric.
- 810 - Step 4: the RF is trained by changing one hyperparameters at once and using
811 the default values for the other three (default values of hyperparameters as
812 reported in Pedegrosa et al (2011) are: `n_estimators=100`; `max_depth=none`,
813 i.e., the tree is expanded until all leaves contain less samples than
814 `min_samples_split`; `min_samples_leaf=1`; `max_features=1`).
- 815 - Step 5: from the results of the previous step, the ranges of hyperparameters,
816 given in table B1, are defined. These values represent the grid in which the
817 optimal hyperparameters are searched. In other words, using the K-fold
818 technique (step 2), RF model is fitted K times, and then the optimal set of
819 values is the one minimizing the RMSE.
- 820 - Step 6 (validation of the model), once the optimal values of the
821 hyperparameters are determined, the performance of RF model is evaluated,
822 for the test dataset as defined in Step 1, using the RMSE.

823 In this study, the described methodology is used to evaluate the hyperparameters
824 for the following RF models: RF1, trained using the input features $\langle H, \theta_6, h_a \rangle$;

825 RF2, trained using $\langle H, \theta_{100}, h_a \rangle$; RF3, trained using $\langle H, \theta_6, \theta_{100} \rangle$; RF4, trained
 826 using $\langle H, \theta_6, \theta_{100} \rangle$. All models are trained to predict the normalized change of
 827 water storage in the soil mantle, $\Delta S/H$. Figures B1, B2, B3 and B4 show the
 828 results of step 4. Specifically, they depict the trends of the RMSE versus the
 829 hyperparameters for RF1, RF2, RF3 and RF4, respectively.

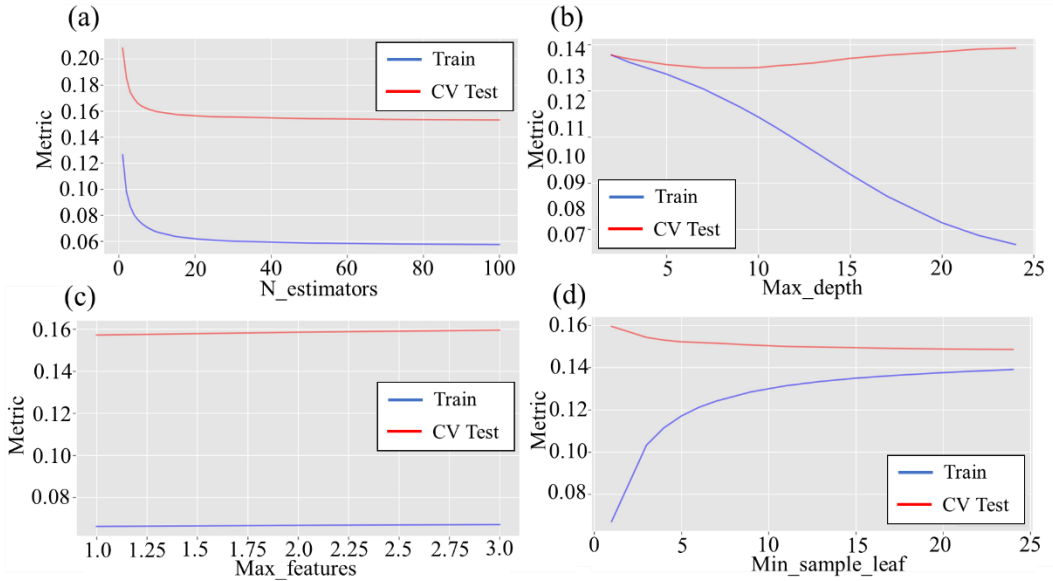


830
 831 **Figure B1. Performance of random forest model RF1 on the test and Cross**
 832 **Validation (CV) sets according to the test metric by changing the hyperparameters:**
 833 **(a) N_estimators (b) Max_depth (c) Max_features (d) Min_samples_leaf**



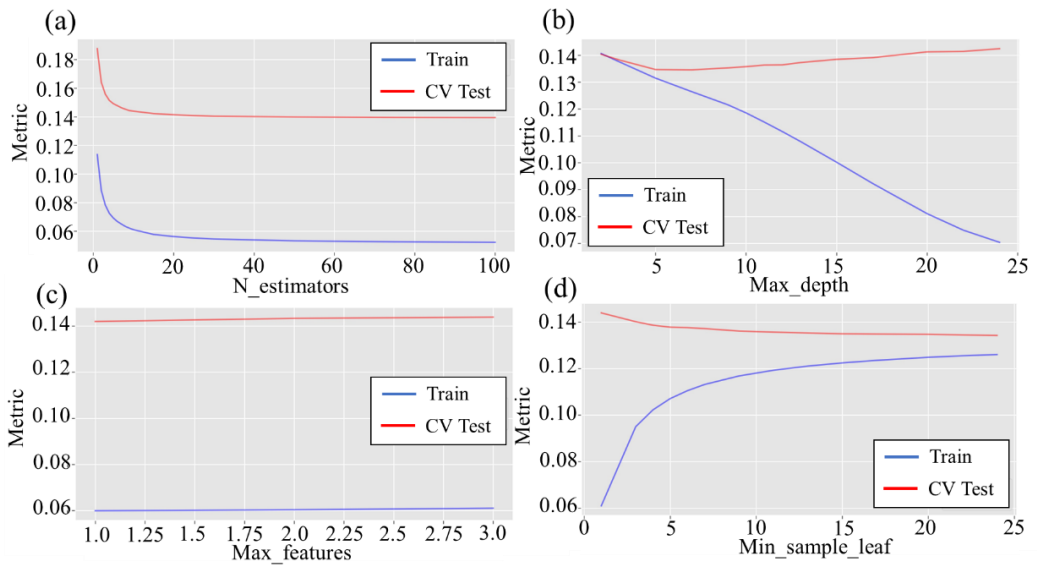
834

835 **Figure B2. Performance of random forest model RF2 on the test and Cross**
 836 **Validation (CV) sets according to the test metric by changing the hyperparameters:**
 837 **(a) N_estimators (b) Max_depth (c) Max_features (d) Min_samples_leaf**



838

839 **Figure B3. Performance of random forest model RF3 on the test and Cross**
 840 **Validation (CV) sets according to the test metric by changing the hyperparameters:**
 841 **(a) N_estimators (b) Max_depth (c) Max_features (d) Min_samples_leaf**



842
 843 **Figure B4. Performance of random forest model RF4 on the test and Cross**
 844 **Validation (CV) sets according to the test metric by changing the hyperparameters:**
 845 **(a) N_estimators (b) Max_depth (c) Max_features (d) Min_samples_leaf**

846 The analysis of the previous figures provides the search grid of hyperparameters
 847 given in Table B1. After fitting each model K times (step 5), the optimal sets of
 848 hyperparameters are reported in Table B2 for each RF model. Then, the
 849 performance of models RF1, RF2, RF3, and RF4 are evaluated on the test dataset
 850 using RMSE metric. The obtained results are summarized in Table B3.

851 The above-described analysis has been used to identify the most informative
 852 triplet of variables, which has been chosen as the one corresponding to the best
 853 performing among the optimal RF models, namely RF2.

854 **Table B1. Hyperparameters range of variation**

Hyperparameter	Range of variation
n_estimators	5,10,20,25,30
max_features	1,2,3
min_samples_leaf	15,20,25
max_depth	3,4, 5, 6,7

855

856 **Table B2. Optimal values of Hyperparameters**

Hyperparameter r	Optimal values			
	RF1	RF2	RF3	RF4
n_estimators	30	30	25	30
max_features	2	2	3	2
min_samples_leaf	20	20	9	20
max_depth	7	7	7	7

857

858 **Table B3. RMSE of studied models computed for the test dataset**

Model	RMSE
RF1 $\langle H, \theta_6, h_a \rangle$	0.122
RF2 $\langle H, \theta_{100}, h_a \rangle$	0.120
RF3 $\langle H, \theta_6, \theta_{100} \rangle$	0.140
RF4 $\langle \theta_6, \theta_{100}, h_a \rangle$	0.124

859

860

861

862 **Author contributions**

863 RG and DR formulated the research aim; PM provided the field measurements;
864 PM and GS supplied the model simulations; DR and GS curated and analyzed
865 the data; RG oversighted the research activities; DR worked on the preparation
866 and the data visualization; DR, PM and GS wrote the draft manuscript; RG wrote
867 the final version of the manuscript.

868 **Acknowledgements**

869 This research is part of the Ph.D. project entitled “Hydrological controls and
870 geotechnical features affecting the triggering of shallow landslides in pyroclastic
871 soil deposits” within the Doctoral Course “A.D.I.” of Università degli Studi della
872 Campania “L. Vanvitelli”.

873 The research has been also funded by Università degli Studi della Campania ‘L.
874 Vanvitelli’ through the programme “VALERE: VAnviteLli pEr la RicErca”.

875 **References**

876 Allocca, V., Manna, F., and De Vita, P.: Estimating annual groundwater recharge
877 coefficient for karst aquifers of the southern Apennines (Italy), *Hydrol Earth Syst*
878 *Sci*, 18, 803–817, <https://doi.org/10.5194/hess-18-803-2014>, 2014.

879 Arthur, D. and Vassilvitskii, S.: k-means++: The Advantages of Careful Seeding,
880 in: *Proceedings of the Eighteenth Annual ACM-SIAM Symposium on Discrete*
881 *Algorithms*, 1027–1035, 2007.

882 Bogaard, T. A. and Greco, R.: Landslide hydrology: from hydrology to pore
883 pressure, *WIREs Water*, 3, 439–459, <https://doi.org/10.1002/wat2.1126>, 2016.

884 Bogaard, T. A. and Greco, R.: Invited perspectives: Hydrological perspectives on
885 precipitation intensity-duration thresholds for landslide initiation: proposing
886 hydro-meteorological thresholds, *Nat. Haz. Earth Sys. Sci.*, 18, 31–39,
887 <https://doi.org/10.5194/nhess-18-31-2018>, 2018.

- 889 Bordoni, M., Meisina, C., Valentino, R., Lu, N., Bittelli, M., and Chersich, S.:
890 Hydrological factors affecting rainfall-induced shallow landslides: From the field
891 monitoring to a simplified slope stability analysis, *Eng. Geol.*,
892 <https://doi.org/10.1016/j.enggeo.2015.04.006>, 2015.
- 893 Breiman, L.: Random Forests, *Mach. Learn.*, 45, 5–32,
894 <https://doi.org/https://doi.org/10.1023/A:1010933404324>, 2001.
- 895 Capretti, P. and Battisti, A.: Water stress and insect defoliation promote the
896 colonization of *Quercus cerris* by the fungus *Biscogniauxia mediterranea*, *For.*
897 *Pathol.*, 37, 129–135, <https://doi.org/10.1111/J.1439-0329.2007.00489.X>, 2007.
- 898 Cascini, L., Cuomo, S., and Guida, D.: Typical source areas of May 1998 flow-
899 like mass movements in the Campania region, Southern Italy, *Eng. Geol.*, 96,
900 107–125, <https://doi.org/10.1016/j.enggeo.2007.10.003>, 2008.
- 901 Cascini, L., Sorbino, G., Cuomo, S., and Ferlisi, S.: Seasonal effects of rainfall
902 on the shallow pyroclastic deposits of the Campania region (southern Italy).
903 *Landslides*, 11(5), 779–792. <https://doi.org/10.1007/s10346-013-0395-3>, 2014.
- 904 Celico, F., Naclerio, G., Bucci, A., Nerone, V., Capuano, P., Carcione, M.,
905 Allocca, V., and Celico, P.: Influence of pyroclastic soil on epikarst formation:
906 A test study in southern Italy, *Terra Nova*, 22, 110–115,
907 <https://doi.org/10.1111/J.1365-3121.2009.00923.X>, 2010.
- 908 Chitu, Z., Bogaard, T. A., Busuioc, A., Burcea, S., Sandric, I., and Adler, M.-J.:
909 Identifying hydrological pre-conditions and rainfall triggers of slope failures at
910 catchment scale for 2014 storm events in the Ialomita Subcarpathians, Romania,
911 *Landslides*, 14, 419–434, <https://doi.org/10.1007/s10346-016-0740-4>, 2017.

912 Comegna, L., Damiano, E., Greco, R., Guida, A., Olivares, L., and Picarelli, L.:
913 Field hydrological monitoring of a sloping shallow pyroclastic deposit, *Can.*
914 *Geotech. J.*, 53, 1125–1137, <https://doi.org/10.1139/cgj-2015-0344>, 2016.

915 Cowpertwait, P. S. P., O’Connell, P. E., Metcalfe, A. V., and Mawdsley, J. A.:
916 Stochastic point process modelling of rainfall. I. Single-site fitting and validation,
917 *J. Hydrol.*, [https://doi.org/10.1016/S0022-1694\(96\)80004-7](https://doi.org/10.1016/S0022-1694(96)80004-7), 1996.

918 Dal Soglio, L., Danquigny, C., Mazzilli, N., Emblanch, C., and Massonnat, G.:
919 Taking into Account both Explicit Conduits and the Unsaturated Zone in Karst
920 Reservoir Hybrid Models: Impact on the Outlet Hydrograph. *Water*, 12, 3221,
921 <https://doi.org/10.3390/w12113221>, 2020.

922 Damiano, E. and Olivares, L.: The role of infiltration processes in steep slope
923 stability of pyroclastic granular soils: laboratory and numerical investigation,
924 *Nat. Haz.*, 52, 329–350, <https://doi.org/10.1007/s11069-009-9374-3>, 2010.

925 Damiano, E., Olivares, L., and Picarelli, L.: Steep-slope monitoring in
926 unsaturated pyroclastic soils, *Eng. Geol.*, 137–138, 1–12,
927 <https://doi.org/10.1016/j.enggeo.2012.03.002>, 2012.

928 Damiano, E., Greco, R., Guida, A., Olivares, L., and Picarelli, L.: Investigation
929 on rainwater infiltration into layered shallow covers in pyroclastic soils and its
930 effect on slope stability, *Eng. Geol.*, 220, 208–218,
931 <https://doi.org/10.1016/j.enggeo.2017.02.006>, 2017.

932 de Amorim, R. C. and Hennig, C.: Recovering the number of clusters in data sets
933 with noise features using feature rescaling factors, *Inf. Sci. (N Y)*, 324, 126–145,
934 <https://doi.org/10.1016/J.INS.2015.06.039>, 2015.

935 De Vita, P., Agrello, D., and Ambrosino, F.: Landslide susceptibility assessment
936 in ash-fall pyroclastic deposits surrounding Mount Somma-Vesuvius:

937 Application of geophysical surveys for soil thickness mapping, *J. Appl.*
938 *Geophys.*, 59, 126–139, <https://doi.org/10.1016/j.jappgeo.2005.09.001>, 2006.

939 Efron, B. and Tibshirani, R.J., *An Introduction to the Bootstrap*. Chapman and
940 Hall, New York. <https://doi.org/10.1007/978-1-4899-4541-9>, 1993.

941 Feddes, R. A., Kowalik, P., Kolinska-Malinka, K., and Zaradny, H.: Simulation
942 of field water uptake by plants using a soil water dependent root extraction
943 function, *J. Hydrol.*, 31, 13–26, [https://doi.org/10.1016/0022-1694\(76\)90017-2](https://doi.org/10.1016/0022-1694(76)90017-2),
944 1976.

945 Fiorillo, F., Guadagno, F., Aquino, S., and De Blasio, A.: The December 1999
946 Cervinara landslides: Further debris flows in the pyroclastic deposits of
947 Campania (Southern Italy), *Bull. Eng. Geol. Env.*,
948 <https://doi.org/10.1007/s100640000093>, 2001.

949 Forestieri, A., Caracciolo, D., Arnone, E., and Noto, L.V.: Derivation of Rainfall
950 Thresholds for Flash Flood Warning in a Sicilian Basin Using a Hydrological
951 Model, *Procedia Engineering*, 154, 818-825, ISSN 1877-7058,
952 <https://doi.org/10.1016/j.proeng.2016.07.413>, 2016.

953 Gao, S. and Shain, L.: Effects of water stress on chestnut blight, *Can. J. For. Res.*,
954 25, 1030–1035, 1995.

955 Greco, R. and Gargano, R.: A novel equation for determining the suction stress
956 of unsaturated soils from the water retention curve based on wetted surface area
957 in pores, *Water Resour Res.*, 51, 6143–6155,
958 <https://doi.org/10.1002/2014WR016541>, 2015.

959 Greco, R., Comegna, L., Damiano, E., Guida, A., Olivares, L., and Picarelli, L.:
960 Hydrological modelling of a slope covered with shallow pyroclastic deposits
961 from field monitoring data, *Hydrol. Earth. Syst. Sci.*, 17, 4001–4013,
962 <https://doi.org/10.5194/hess-17-4001-2013>, 2013.

963 Greco, R., Comegna, L., Damiano, E., Guida, A., Olivares, L., and Picarelli, L.:
964 Conceptual Hydrological Modeling of the Soil-bedrock Interface at the Bottom
965 of the Pyroclastic Cover of Cervinara (Italy), *Procedia Earth and Planetary*
966 *Science*, <https://doi.org/10.1016/j.proeps.2014.06.007>, 2014.

967 Greco, R., Marino, P., Santonastaso, G. F., and Damiano, E.: Interaction between
968 Perched Epikarst Aquifer and Unsaturated Soil Cover in the Initiation of Shallow
969 Landslides in Pyroclastic Soils, *Water*, 10, 948,
970 <https://doi.org/10.3390/w10070948>, 2018.

971 Greco, R., Comegna, L., Damiano, E., Marino, P., Olivares, L., and Santonastaso,
972 G. F.: Recurrent rainfall-induced landslides on the slopes with pyroclastic cover
973 of Partenio Mountains (Campania, Italy): Comparison of 1999 and 2019 events,
974 *Eng Geol*, 288, 106160, <https://doi.org/10.1016/j.enggeo.2021.106160>, 2021.

975 Greco, R., Marino, P., and Bogaard, T. A.: Recent Advancements of Landslide
976 Hydrology, *WIREs Water*, e1675. <https://doi.org/10.1002/wat2.1675>, 2023.

977 Hartmann, A., Goldscheider, N., Wagener, T., Lange, J., and Weiler, M.: Karst
978 water resources in a changing world: Review of hydrological modeling
979 approaches, *Reviews of Geophysics*, 52, 218–242,
980 <https://doi.org/10.1002/2013RG000443>, 2014.

981 Hastie, T., Tibshirani, R., and Friedman, J.: *The Elements of Statistical Learning*
982 *Data Mining, Inference, and Prediction*, 2nd ed., Springer Series on Statistics,
983 Stanford, 1–763 pp., 2008.

984 Lloyd, S. P.: Least Squares Quantization in PCM, *IEEE Trans. Inf. Theory*, 28,
985 1982.

986 Lu, N. and Likos, W. J.: Suction Stress Characteristic Curve for Unsaturated Soil,
987 *J. Geotech. Geoenv. Eng.*, [https://doi.org/10.1061/\(asce\)1090-](https://doi.org/10.1061/(asce)1090-0241(2006)132:2(131))
988 [0241\(2006\)132:2\(131\)](https://doi.org/10.1061/(asce)1090-0241(2006)132:2(131)), 2006.

989 Marino, P., Comegna, L., Damiano, E., Olivares, L., and Greco, R.: Monitoring
990 the Hydrological Balance of a Landslide-Prone Slope Covered by Pyroclastic
991 Deposits over Limestone Fractured Bedrock, *Water*, 12, 3309,
992 <https://doi.org/10.3390/w12123309>, 2020a.

993 Marino, P., Peres, D.J., Cancelliere, A., Greco, R. and Bogaard, T. A.: Soil
994 moisture information can improve shallow landslide forecasting using the
995 hydrometeorological threshold approach, *Landslides* 17, 2041–2054,
996 <https://doi.org/10.1007/s10346-020-01420-8>, 2020b.

997 Marino, P., Santonastaso, G. F., Fan, X., and Greco, R.: Prediction of shallow
998 landslides in pyroclastic-covered slopes by coupled modeling of unsaturated and
999 saturated groundwater flow, *Landslides*, [https://doi.org/10.1007/s10346-020-](https://doi.org/10.1007/s10346-020-01484-6)
1000 01484-6, 2021.

1001 McDowell, N., Pockman, W. T., Allen, C. D., Breshears, D. D., Cobb, N., Kolb,
1002 T., Plaut, J., Sperry, J., West, A., Williams, D. G., and Yezpe, E. A.: Mechanisms
1003 of plant survival and mortality during drought: Why do some plants survive while
1004 others succumb to drought?, *New Phytologist*, 178, 719–739,
1005 <https://doi.org/10.1111/J.1469-8137.2008.02436.X>, 2008.

1006 Nieber, J. L. and Sidle, R. C.: How do disconnected macropores in sloping soils
1007 facilitate preferential flow?, *Hydrol. Process.*, 24, 1582–1594,
1008 <https://doi.org/10.1002/hyp.7633>, 2010.

1009 Olivares, L. and Picarelli, L.: Shallow flowslides triggered by intense rainfalls on
1010 natural slopes covered by loose unsaturated pyroclastic soils, *Geotechnique*,
1011 <https://doi.org/10.1680/geot.2003.53.2.283>, 2003.

1012 Pagano, L., Picarelli, L., Rianna, G., and Urciuoli, G.: A simple numerical
1013 procedure for timely prediction of precipitation-induced landslides in unsaturated

1014 pyroclastic soils, *Landslides*, 7, 273–289, <https://doi.org/10.1007/s10346-010->
1015 0216-x, 2010.

1016 Pan, S., Pan, N., Tian, H., Friedlingstein, P., Sitch, S., Shi, H., Arora, V. K.,
1017 Haverd, V., Jain, A. K., Kato, E., Lienert, S., Lombardozzi, D., Nabel, J. E. M.
1018 S., Ottlé, C., Poulter, B., Zaehle, S., and Running, S. W.: Evaluation of global
1019 terrestrial evapotranspiration using state-of-the-art approaches in remote sensing,
1020 machine learning and land surface modeling, *Hydrol. Earth. Syst. Sci.*, 24, 1485–
1021 1509, <https://doi.org/10.5194/hess-24-1485-2020>, 2020.

1022 Paulik, C., Dorigo, W., Wagner, W., and Kidd, R.: Validation of the ASCAT Soil
1023 Water Index using in situ data from the International Soil Moisture Network, *Int.*
1024 *J. Appl. Earth Obs. . Geoinf.*, 30, 1–8,
1025 <https://doi.org/10.1016/J.JAG.2014.01.007>, 2014.

1026 Pedregosa, F., Varoquaux, G., Gramfort, A., Michel, V., Thirion, B., Grisel, O.,
1027 Blondel, M., Prettenhofer, P., Weiss, R., Dubourg, V., Vanderplas, J., Passos, A.,
1028 Cournapeau, D., Brucher, M., Perrot, M., and Duchesnay, E.: Scikit-learn:
1029 Machine Learning in Python. *J. Mach. Lear. Res.*, 12, 2825–2830, 2011.

1030 Peres, D. J. and Cancelliere, A.: Derivation and evaluation of landslide-triggering
1031 thresholds by a Monte Carlo approach, *Hydrol. Earth Syst. Sci.*, 18, 4913–4931,
1032 <https://doi.org/10.5194/hess-18-4913-2014>, 2014.

1033 Peres, D. J., Cancelliere, A., Greco, R., and Bogaard, T. A.: Influence of uncertain
1034 identification of triggering rainfall on the assessment of landslide early warning
1035 thresholds, *Nat. Hazards Earth. Syst. Sci.*, 18, 633–646,
1036 <https://doi.org/10.5194/nhess-18-633-2018>, 2018.

1037 Perrin, J., Jeannin, P. Y., and Zwahlen, F.: Epikarst storage in a karst aquifer: A
1038 conceptual model based on isotopic data, Milandre test site, Switzerland. *J.*

- 1039 Hydrol., 279(1-4), 106-124, [https://doi.org/10.1016/S0022-1694\(03\)00171-9](https://doi.org/10.1016/S0022-1694(03)00171-9),
1040 2003.
- 1041 Pirone, M., Papa, R., Nicotera, M. V., and Urciuoli, G.: Soil water balance in an
1042 unsaturated pyroclastic slope for evaluation of soil hydraulic behaviour and
1043 boundary conditions, *J. Hydrol.*, <https://doi.org/10.1016/j.jhydrol.2015.06.005>,
1044 2015.
- 1045 Ponce, V. M. and Hawkins, R. H.: Runoff Curve Number: Has It Reached
1046 Maturity?, *J. Hydrol. Eng.*, 1, 11–19, [https://doi.org/10.1061/\(ASCE\)1084-
1047 0699\(1996\)1:1\(11\)](https://doi.org/10.1061/(ASCE)1084-0699(1996)1:1(11)), 1996.
- 1048 Revellino, P., Guerriero, L., Gerardo, G., Hungr, O., Fiorillo, F., Esposito, L.,
1049 and Guadagno, F. M.: Initiation and propagation of the 2005 debris avalanche at
1050 Nocera Inferiore (Southern Italy), *Ital. J. Geosci.*,
1051 <https://doi.org/10.3301/IJG.2013.02>, 2013.
- 1052 Reichenbach, P., Cardinali, M., De Vita, P., and Guzzetti, F.: Regional
1053 hydrological thresholds for landslides and floods in the Tiber River Basin (central
1054 Italy), *Environ. Geol.*, 35, 146–159, <https://doi.org/10.1007/s002540050301>,
1055 1998.
- 1056 Richards, L. A.: Capillary conduction of liquids through porous mediums, *J.*
1057 *Appl. Phys.*, <https://doi.org/10.1063/1.1745010>, 1931.
- 1058 Rodriguez-Iturbe, I., Febres De Power, B., and Valdes, J. B.: Rectangular pulses
1059 point process models for rainfall: analysis of empirical data, *J. Geophys. Res.*,
1060 <https://doi.org/10.1029/JD092iD08p09645>, 1987.
- 1061 Rolandi, G., Bellucci, F., Heizler, M. T., Belkin, H. E., and De Vivo, B.: Tectonic
1062 controls on the genesis of ignimbrites from the Campanian Volcanic Zone,
1063 southern Italy, *Miner. Petrol.*, 79, 3–31, [https://doi.org/10.1007/s00710-003-
1064 0014-4](https://doi.org/10.1007/s00710-003-0014-4), 2003.

1065 Rousseeuw, P. J.: Silhouettes: A graphical aid to the interpretation and validation
1066 of cluster analysis, *J. Comput. Appl. Math.*, 20, 53–65,
1067 [https://doi.org/10.1016/0377-0427\(87\)90125-7](https://doi.org/10.1016/0377-0427(87)90125-7), 1987.

1068 Segoni, S., Piciullo, L. and Gariano, S.L.: A review of the recent literature on
1069 rainfall thresholds for landslide occurrence, *Landslides*, 15, 1483–1501,
1070 <https://doi.org/10.1007/s10346-018-0966-4>, 2018.

1071 Shuttleworth, W. J.: Evaporation, in: *Handbook of Hydrology*, edited by:
1072 Maidment, D. R., McGraw-Hill, New York, NY, USA, 1993.

1073 Stone M.: Cross-validatory choice and assessment of statistical predictions. *J.*
1074 *Royal Stat. Soc.*, 36(2), 111–147, 1974.

1075 Tromp-Van Meerveld, H. J. and McDonnell, J. J.: Threshold relations in
1076 subsurface stormflow: 1. A 147-storm analysis of the Panola hillslope, *Water*
1077 *Resour. Res.*, 42, 2410, <https://doi.org/10.1029/2004WR003778>, 2006a.

1078 Tromp-Van Meerveld, H. J. and McDonnell, J. J.: Threshold relations in
1079 subsurface stormflow: 2. The fill and spill hypothesis, *Water Resour. Res.*,
1080 <https://doi.org/10.1029/2004WR003800>, 2006b.

1081 Tufano, R., Formetta, G., Calcaterra, D., and De Vita, P.: Hydrological control
1082 of soil thickness spatial variability on the initiation of rainfall-induced shallow
1083 landslides using a three-dimensional model, *Landslides*, 18, 3367-3380,
1084 <https://doi.org/10.1007/s10346-021-01681-x>, 2021.

1085 Twarakavi, N. K. C., Sakai, M., and Šimůnek, J.: An objective analysis of the
1086 dynamic nature of field capacity, *Water Resour. Res.*, 45,
1087 <https://doi.org/10.1029/2009WR007944>, 2009.

1088 van Genuchten, M. Th.: A Closed-form Equation for Predicting the Hydraulic
1089 Conductivity of Unsaturated Soils¹, *Soil Sci. Soc. Am. J.*, 44, 892,
1090 <https://doi.org/10.2136/sssaj1980.03615995004400050002x>, 1980.

1091 Wicki, A., Lehmann, P., Hauck, C., Seneviratne, S. I., Waldner, P., and Stähli,
1092 M.: Assessing the potential of soil moisture measurements for regional landslide
1093 early warning, *Landslides*, 17, 1881–1896, <https://doi.org/10.1007/S10346-020->
1094 01400-Y, 2020.

1095 Williams, P. W.: The role of the epikarst in karst and cave hydrogeology: a
1096 review, *Int. J. Speleol.*, 37, 1–10, <https://doi.org/10.5038/1827-806X.37.1.1>,
1097 2008.

1098